Article

Signatures of bosonic Landau levels in a finite-momentum superconductor

https://doi.org/10.1038/s41586-021-03915-3

Received: 15 February 2021

Accepted: 16 August 2021

Published online: 3 November 2021

Check for updates

A. Devarakonda[1], T. Suzuki[1,7], S. Fang[2], J. Zhu[1], D. Graf[3], M. Kriener[4], L. Fu[1], E. Kaxiras[5,6] & J. G. Checkelsky[1]✉

Charged particles subjected to magnetic fields form Landau levels (LLs). Originally studied in the context of electrons in metals[1], fermionic LLs continue to attract interest as hosts of exotic electronic phenomena[2,3]. Bosonic LLs are also expected to realize novel quantum phenomena[4,5], but, apart from recent advances in synthetic systems[6,7], they remain relatively unexplored. Cooper pairs in superconductors—composite bosons formed by electrons—represent a potential condensed-matter platform for bosonic LLs. Under certain conditions, an applied magnetic field is expected to stabilize an unusual superconductor with finite-momentum Cooper pairs[8,9] and exert control over bosonic LLs[10–13]. Here we report thermodynamic signatures, observed by torque magnetometry, of bosonic LL transitions in the layered superconductor $Ba_6Nb_{11}S_{28}$. By applying an in-plane magnetic field, we observe an abrupt, partial suppression of diamagnetism below the upper critical magnetic field, which is suggestive of an emergent phase within the superconducting state. With increasing out-of-plane magnetic field, we observe a series of sharp modulations in the upper critical magnetic field that are indicative of distinct vortex states and with a structure that agrees with predictions for Cooper pair LL transitions in a finite-momentum superconductor[10–14]. By applying Onsager's quantization rule[15], we extract the momentum. Furthermore, study of the fermionic LLs shows evidence for a non-zero Berry phase. This suggests opportunities to study bosonic LLs, topological superconductivity, and their interplay via transport[16], scattering[17], scanning probe[18] and exfoliation techniques[19].

The distinctive properties of Landau levels (LLs) can be traced to the single-valuedness of a quantum mechanical particle's wavefunction along closed orbits (Fig. 1a, top). For electrons undergoing cyclotron motion, this is encoded in Onsager's quantization rule $\mathcal{A}_k\ell^2 = 2\pi(n+\gamma)$, where $\mathcal{A}_k$ is the momentum space area enclosed by the orbit, $\ell = \sqrt{\hbar/eB}$ is the magnetic length (with $\hbar$ and e the reduced Planck constant and elementary charge, respectively) set by the magnetic induction $\mathbf{B} = \nabla \times \mathbf{A}$ from the vector potential $\mathbf{A}$, n is the LL index, and the phase $\gamma = 1/2$ in conventional metals arising from quantum corrections[15]. This discretizes continuous energy bands and, semiclassically, enforces magnetic flux quantization such that LLs enclose an integer number of flux quanta $\Phi_0 = h/e$. In two dimensions, the resulting flatbands have a topological classification that can be explored using a magnetic field or electron filling. Systems that host synthetic magnetic fields $\nabla \times \mathbf{\Omega}$, where $\mathbf{\Omega}$ is an underlying gauge field, with particles executing closed orbits can also host LLs (Fig. 1a, bottom). For example, recent work has demonstrated bosonic particles in LLs using $\nabla \times \mathbf{\Omega}$ generated by twist angle Θ in non-coplanar photonic resonators[6] and rotation ω in ultracold atom traps[7]. However, Bose–Einstein statistics favour occupation of the ground state $n = 0$ LL, posing an impediment to accessing the higher $n > 0$ levels where two-dimensional (2D) fermionic LLs show topologically ordered[20] and symmetry-broken[21] states.

Although the superconducting proximity effect has been employed to form Cooper pairs—spatially extended composite bosons formed by paired electrons—in LLs[22], 2D finite-momentum (finite-q) superconductors (SCs) may intrinsically support higher n and bosonic LLs more broadly. In conventional (Bardeen–Cooper–Schrieffer (BCS)) 2D SCs, ψ, the order parameter characterizing the Cooper pair wavefunction, is constant whereas the hallmark of finite-q superconductivity is a periodic variation of ψ. An example is the Fulde–Ferrell–Larkin–Ovchinnikov (FFLO) state[8–10], which can host periodic stripe-like nodes in ψ driven by a magnetic field (H) such that the Zeeman energy of unpaired electrons equals the pairing energy Δ_{SC} (the Pauli-limit $\mu_0 H_P = 1.84\,T_c$, where μ_0, H_P and T_c are the vacuum permeability, Pauli-limit field and superconducting transition temperature, respectively). Although pairing is often suppressed in three-dimensional SCs below H_P by orbital limiting, this mechanism is weaker in 2D SCs for H applied in-plane, potentially making this limit accessible[23]. In this case, it is possible for BCS superconductivity with constant ψ (Fig. 1b, left) to be superseded by the finite-q state (Fig. 1b, right). This is due to competition between curvature

[1]Department of Physics, Massachusetts Institute of Technology, Cambridge, MA, USA. [2]Department of Physics and Astronomy, Center for Materials Theory, Rutgers University, Piscataway, NJ, USA. [3]National High Magnetic Field Laboratory, Tallahassee, FL, USA. [4]RIKEN Center for Emergent Matter Science (CEMS), Wako, Japan. [5]Department of Physics, Harvard University, Cambridge, MA, USA. [6]John A. Paulson School of Engineering and Applied Sciences, Harvard University, Cambridge, MA, USA. [7]Present address: Department of Physics, Toho University, Funabashi, Japan. ✉e-mail: checkelsky@mit.edu

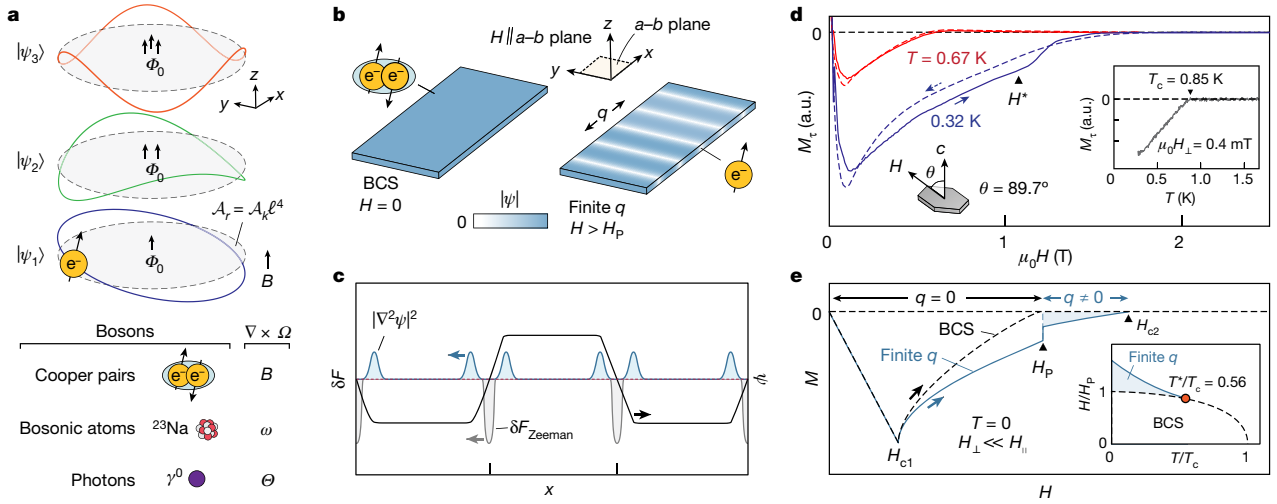

Fig. 1 | Bosonic LLs, finite-q superconductivity and torque magnetization of $Ba_6Nb_{11}S_{28}$. a, Top, schematic single-valued wavefunctions $|\psi_1\rangle$, $|\psi_2\rangle$ and $|\psi_3\rangle$ enclosing area $\mathcal{A}_r = \mathcal{A}_k \ell^4$, threaded by flux Φ_0, $2\Phi_0$ and $3\Phi_0$, respectively. Bottom, bosonic particles such as Cooper pairs, certain atoms or photons can be driven into LLs using **B**, rotation ω or twist angle Θ, respectively. **b**, Two-dimensional BCS superconductivity with uniform ψ (left) transitions to finite-q pairing with periodic nodes in ψ (right) when an external field $H > H_P$ is applied parallel to the a–b plane. **c**, Although deformations in ψ (black) incur a free-energy cost (blue), the Zeeman energy gained by spin-polarized, unpaired electrons where $\psi = 0$ stabilizes finite-q pairing. **d**, Up and down sweeps of $M_\tau(H)$ for $\theta = 89.7°$ (measured relative to the c axis), solid and dashed lines, respectively, at $T = 0.32$ K (blue) and $T = 0.67$ K (red). Inset, $M_\tau(T)$ measured with $\mu_0 H_\perp = 0.4$ mT, where diamagnetism is seen below the superconducting transition at $T_c = 0.85$ K. **e**, For $T = 0$ and $H_\perp \ll H_\parallel$, finite-q SCs exhibit an abrupt increase in $M(H)$ at H_P as unpaired, spin-polarized electrons emerge entering the finite-q state (blue, shaded). Conventional SCs show a smooth evolution of $M(H)$ between H_{c1} and H_{c2} (black). Inset, the T–H phase diagram of finite-q pairing in 2D SCs. Finite-q pairing is accessible below $T^* = 0.56T_c$.

of ψ with a free-energy cost $\delta F \propto |\nabla^2\psi|^2$ (Methods) and the Zeeman energy δF_{Zeeman} from spin polarization of unpaired electrons where $\psi = 0$ (Fig. 1c)[24]. Additional factors, such as unconventional pairing or structural anisotropy[25], can yield different spatial patterns (Methods). Across these, δF_{Zeeman} permits the finite-q state and control over LLs[10–13].

Emergent superconducting state

The formation of nodes in ψ is imprinted on thermodynamic quantities such as heat capacity and magnetization M. There is a long and rich history of work searching for finite-q pairing with a variety of approaches used to overcome the challenging requirements for material quality and experimental sophistication to measure q (refs. [26,27]). Here we examine the magnetization response M_τ of the layered 2D SC $Ba_6Nb_{11}S_{28}$ (ref. [28]) using torque magnetometry (data shown for representative sample S1 unless noted, Methods). Superconductivity in $Ba_6Nb_{11}S_{28}$ below $T_c = 0.85$ K is marked by the onset of diamagnetism in $M_\tau(T)$ measured with a small out-of-plane H component $\mu_0 H_\perp = 0.4$ mT (Fig. 1d, inset). Type II superconductivity is evident with $M_\tau(H)$ measured with H oriented at $\theta = 89.7°$ relative to the c axis at fixed $T = 0.67$ K (Fig. 1d, red) and 0.32 K (Fig. 1d, blue), showing a mixed state between the lower critical field where M_τ reaches a minimum and the upper critical field where superconductivity is suppressed, $\mu_0 H_{c1} = 0.12$ T and $\mu_0 H_{c2} = 1.37$ T, respectively, at 0.32 K (Methods). For increasing H at $T = 0.32$ K (Fig. 1d, solid blue), we see an abrupt increase of M_τ with onset at an intermediate field $\mu_0 H^* = 1.04$ T. At the same T, M_τ measured with decreasing H from the normal state above H_{c2} (Fig. 1d, dashed blue) shows hysteresis. In contrast, $M_\tau(H)$ at $T = 0.67$ K (Fig. 1d, red solid and dashed) is featureless for $H_{c1} < H < H_{c2}$ and the abrupt hysteresis is absent.

Given that the diamagnetic response of SCs scales with the superconducting volume fraction[29], the decrease in $|M_\tau|$ at H^* for $T = 0.32$ K points to an emergent phase with a reduced volume fraction within the superconducting state (Methods). This contrasts with prototypical BCS SCs where M exhibits perfect diamagnetism until the lower critical field H_{c1} followed by a continuous decrease of $|M|$ until H_{c2} where superconductivity is extinguished (Fig. 1e, black dashed). Instead, this would be consistent with a finite-q phase where the reduced superconducting volume fraction from the formation of nodes in ψ is imprinted on M (Fig. 1e, blue solid)[30]. The more conventional $M_\tau(H)$ at $T = 0.67$ K $\approx 0.8T_c$ aligns with calculations showing that the 2D finite-q state appears below a characteristic temperature $T^* \approx 0.56T_c$ (see phase diagram, Fig. 1e, inset).

We measured $M_\tau(H)$ for $\theta = 89.7°$ at additional fixed T to construct a phase diagram of these features. As shown in Fig. 2a, an abrupt increase in $M_\tau(H)$ and associated hysteresis in H is apparent for $T \lesssim 0.4$ K. Figure 2b collects the results for H_{c1}, H^* and H_{c2} for $\theta = 89.7°$ in T and H, suggesting $T^* = 0.44$ K $= 0.52T_c$ (Methods), consistent with the predicted $T^* = 0.56T_c$. We find that $H^*(T)$ and $H_{c2}(T > T^*)$ follow the usual 2D Ginzburg–Landau (2D-GL) model of H_{c2}, $H_{c2}(T) = H_{c2}(0)\sqrt{1 - T/T_c}$ with $\mu_0 H_{c2}(0) = 1.28 \pm 0.05$ T, expected from the high-temperature behaviour $H_{c2}(T/T_c > 0.7)$ (Fig. 2b, dashed line and shaded region the fitting uncertainty) above which conventional pairing is unstable. Although spin–orbit scattering[31] or Ising spin–orbit coupling (SOC)[32] may cause deviations of H_{c2} from the 2D-GL model, these run counter to the clean-limit nature of superconductivity[28] and weakened Ising SOC (Methods) in $Ba_6Nb_{11}S_{28}$, respectively, and they do not explain the reduction in SC volume fraction at H^* and its onset at T^*. Instead, this points to a distinct field-induced state bounded by $H^*(T) < H < H_{c2}$ and $T < 0.44$ K, consistent with the expected phase diagram (Fig. 1e, inset, Methods).

At lower $T = 20$ mK and $\theta = 89.7°$, we observe a sharper increase in the up sweep of $M_\tau(H)$ (Fig. 2c) at $\mu_0 H^* = 1.5$ T between $\mu_0 H_{c1} = 0.1$ T and $\mu_0 H_{c2} = 1.75$ T. In addition, the down sweep manifests a dip near H^* at $\mu_0 H' = 1.18$ T, which evolves together with H^* (Methods). The sharp jump and hysteresis in $M_\tau(H)$ suggests that the BCS and field-induced states are separated by a first-order transition with a metastable region between H' and H^*, which brackets $\mu_0 H^*(T = 0) \approx 1.3$ T from the high-T 2D-GL fit (Fig. 2b, Methods). For $H_{c1} \lesssim H \lesssim 1$ T, both up and down sweeps

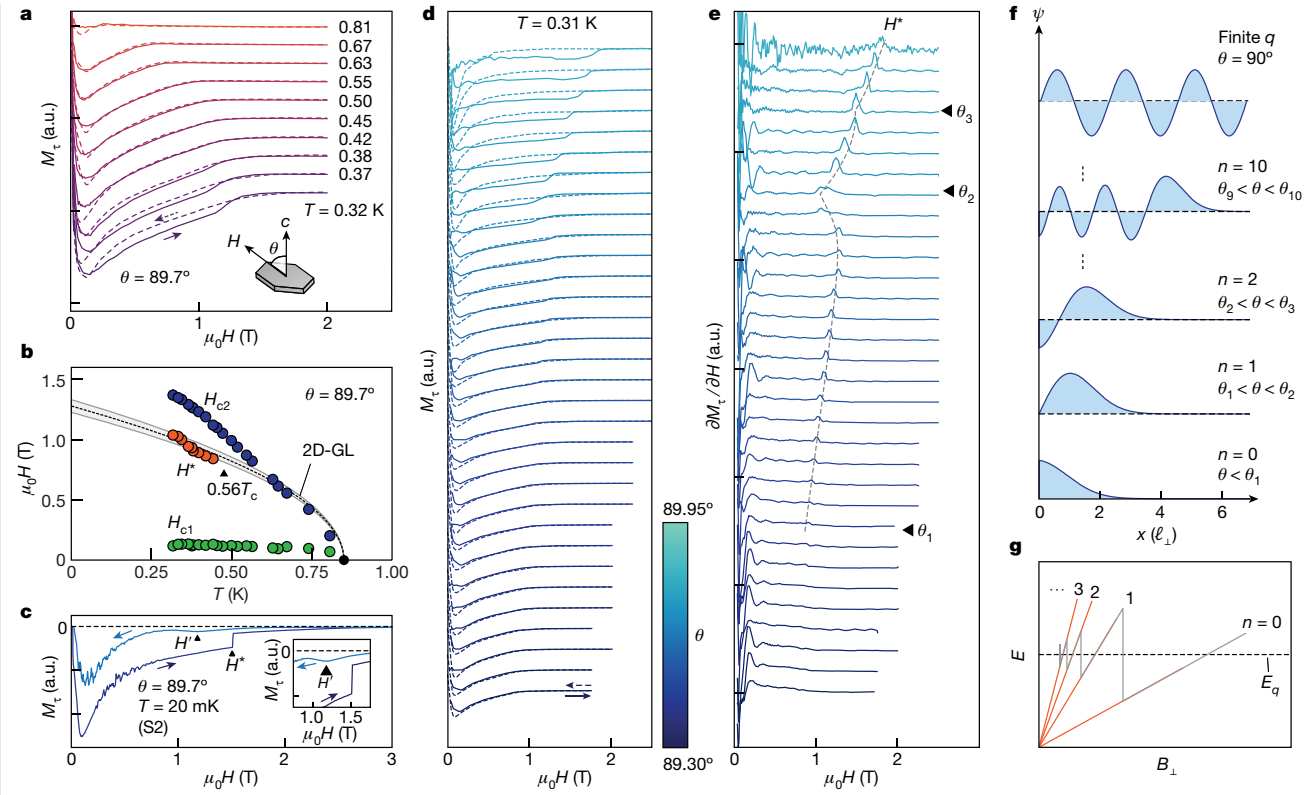

Fig. 2 | Evidence of an emergent superconducting state. a, Up (solid) and down (dashed) sweeps of $M_\tau(H)$ for $\theta = 89.7°$ at various fixed T between 0.81 K and 0.32 K, vertically offset for clarity. **b**, T–H superconducting phase diagram at $\theta = 89.7°$ showing H_{c1} (green), H^* (orange) and H_{c2} (blue). Two-dimensional GL fit of $H^*(T)$ and $H_{c2}(T > T^*)$ (black dashed, fitting uncertainty shown as shaded region) highlights the emergent superconducting state between H^* and H_{c2}. **c**, Up (dark blue) and down (light blue) sweeps of $M_\tau(H)$ at $T = 20$ mK for $\theta = 89.7°$ (sample S2). Inset, a dip-like feature is seen in the down sweep of $M_\tau(H)$ at $\mu_0 H' = 1.18$ T. **d**, Up (solid) and down (dashed) sweeps of $M_\tau(H)$ for $T = 0.31$ K at equally spaced, fixed θ between 89.30° and 89.95°, vertically offset for clarity. **e**, $\partial M_\tau(H)/\partial H$ of up-sweep $M_\tau(H)$ in **d**, vertically offset for clarity. Guide to the eye (grey dashed line) traces the corrugation of $H^*(\theta)$. **f**, Cooper pair transitions between LLs are anticipated as δF_{Zeeman} favours increasingly oscillatory ψ as $\theta \to 90°$ ($\ell_\perp$ is the Cooper pair magnetic length). **g**, Analogous to fermionic systems with E_F, Cooper pairs with kinetic energy E_q undergo LL transitions with increasing $H_\perp$.

show jagged features (Fig. 2c), which may arise from flux jumps (Methods). Their distinct field regime and absence at higher T (Methods) separate them from the behaviour of M_τ near H^* (the organic finite-q SC candidate κ-$(ET)_2Cu(NCS)_2$, where ET is bis(ethylenedithio)tetrathiafulvalene, shows similar behaviour[33]). Furthermore, although vortex physics can have a role, the features in $M_\tau(H)$ are qualitatively distinct from phenomena such as the peak effect in $CeRu_2$ (ref. [34]; Methods).

Signatures of bosonic LL transitions

A fine-grained view of the angular dependent response of $M_\tau(H)$ is shown in Fig. 2d at $T = 0.31$ K for equally spaced, fixed θ between 89.30° and 89.95° (vertically offset for clarity). Analogous to T^*, there is a critical angle above which hysteresis and the abrupt increase in M_τ appear (Fig. 2d solid and dashed lines, up and down sweeps, respectively). Examining the derivative $\partial M_\tau(H)/\partial H$ of the up-sweep traces (Fig. 2e, vertically offset for clarity), we see that the abrupt increase in M_τ appears as a peak in $\partial M_\tau(H)/\partial H$ for $\theta > \theta_1 \approx 89.5°$ (Fig. 2e, black arrows). As $\theta \to 90°$, H^* (Fig. 2e, dashed guide to the eye) shows prominent cusps at $\theta_2 \approx 89.8°$ and $\theta_3 \approx 89.9°$. The non-monotonic θ dependence is inconsistent with the peak effect[35] and generally, the smooth variation expected in conventional SCs[29] (Methods).

Instead, the evidence for a first-order transition and this peculiar angular variation recalls the predicted sequence of LL transitions as ψ evolves from the Abrikosov lattice at $\theta = 0°$ built from $n = 0$ LLs to the finite-q state at $\theta = 90°$ (refs. [10–14,36]). This is driven by δF_{Zeeman} which favours nodes in ψ and increasingly oscillatory LLs (Fig. 2f), causing discrete changes in n at θ_i as $\theta \to 90°$; the sharp features in $H^*(\theta)$ are suggestive of changes in n. Near H_{c2}, this can be recast in the language of fermionic LLs (Methods). From an isotropic 2D finite-q state at $\theta = 90°$ ($H_\perp = 0$) with Cooper pairs carrying kinetic energy $E_q = \hbar^2 q^2/4m^*$ (Fig. 2g, dashed line), where $2m^*$ is the Cooper pair effective mass, application of $H_\perp \neq 0$ drives cyclotron motion and the formation of LLs with energies $E_n = \hbar\omega_c(n + 1/2)$ (Fig. 2g, orange lines) where $\omega_c = e\mu_0 H_\perp/m^*$ is the cyclotron frequency. With increasing $H_\perp$, Cooper pairs transition between LLs as they minimize free energy analogous to fermionic systems[13], except here, E_q replaces the Fermi energy E_F. Theory also predicts that $H_{c2}(\theta)$ across these LL transitions will show corrugations that can be used to extract q (refs. [10–13]). The prominent features seen here indicate that this system is near the 2D isotropic limit, suggesting that q may be obtained from $H_{c2}(\theta)$ (ref. [25]; Methods).

To look for these signatures, we mapped $H_{c2}(\theta, T)$ for $T = 310$ mK, 395 mK, 460 mK and 600 mK, as shown in Fig. 3a. Although $H_{c2}(\theta)$ evolves monotonically at $T = 600$ mK, corrugations become apparent and increasingly prominent as T is lowered. At 310 mK, we identify three transitions, the first at $\theta_1 = 89.513° \pm 0.007°$ determined from $\partial M_\tau(H)/\partial H$ (Fig. 2e, black arrows, Fig. 3a, dashed vertical lines), followed by minima in $H_{c2}(\theta)$ at $\theta_2 = 89.804° \pm 0.004°$ and $\theta_3 = 89.872° \pm 0.004°$

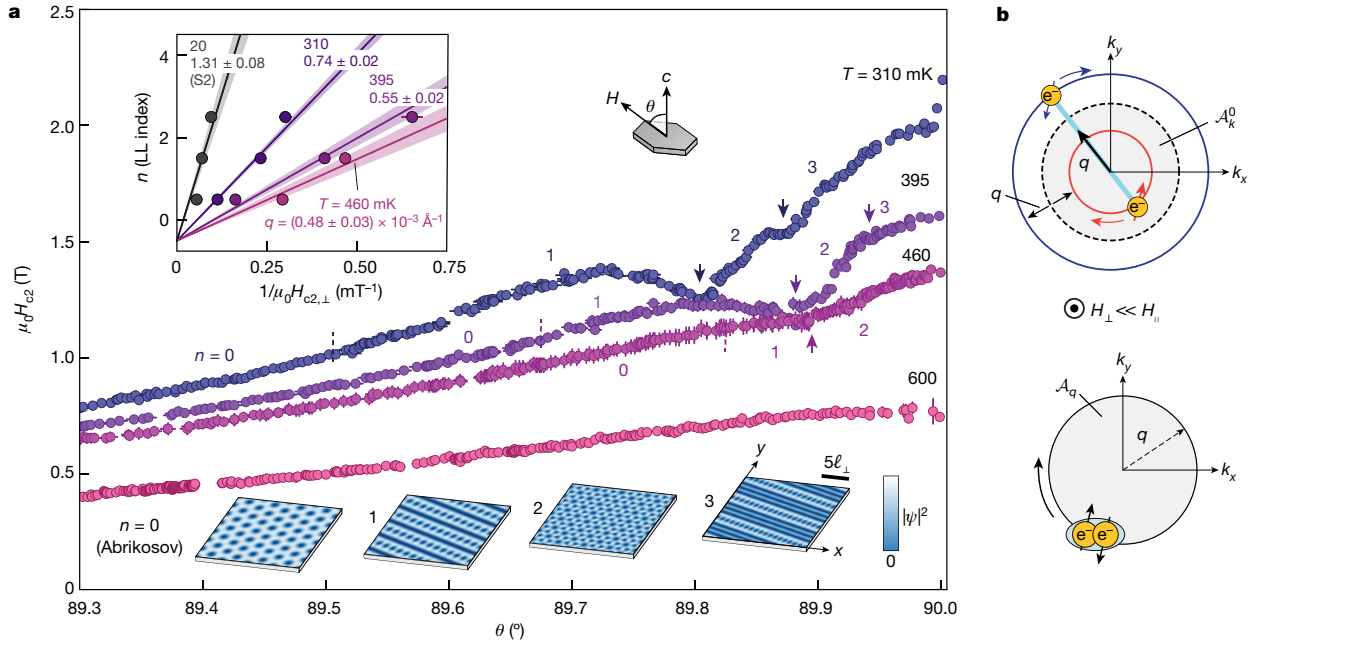

Fig. 3 | Signatures of bosonic LL transitions. a, $H_{c2}(\theta)$ near $\theta = 90°$ at $T = 310$ mK, $T = 395$ mK, $T = 460$ mK and $T = 600$ mK. Transitions into the $n = 1$ and successively higher LLs are marked by dashed vertical lines and closed arrows, respectively. Top inset, bosonic LL index plot constructed from transitions observed at $T = 20$ mK (sample S2), $T = 310$ mK, $T = 395$ mK and $T = 460$ mK. Fitting uncertainties are indicated by the shaded regions. Bottom inset, LL transitions seed abrupt changes in the spatial structure of $|\psi|$. **b**, Top, electrons on Zeeman-split FSs, separated by q enclosing $\mathcal{A}_k^0$, undergo cyclotron motion when subject to $H_\perp$. Bottom, Cooper pairs formed across these FSs acquire finite q and undergo cyclotron motion enclosing area $\mathcal{A}_q$.

(Fig. 3a, closed arrows). At higher T, we identify three and two transitions at 395 mK and 460 mK, respectively.

Semiclassically, $H_\perp$ drives cyclotron motion of spin-up and spin-down electrons along Fermi surfaces (FSs) Zeeman split by q (Fig. 3b, top orange and blue, respectively) from the $H = 0$ FS enclosing an area $\mathcal{A}_k^0$ (Fig. 3b, top grey shaded). Cooper pairs formed between these FSs acquire finite q and also undergo cyclotron motion, enclosing an area $\mathcal{A}_q$ (Fig. 3b, bottom). This suggests a Cooper pair counterpart to Onsager's rule

$$\mathcal{A}_q \ell_\perp^2 = 2\pi(n + 1/2) \quad (1)$$

with the Cooper pair magnetic length $\ell_\perp = \sqrt{\hbar/(2e\mu_0 H_\perp)}$ (Methods). Assuming an isotropic Cooper pair orbit with $\mathcal{A}_q = \pi q^2$, we perform an index analysis analogous to that for fermionic quantum oscillations (QOs) to extract q from the slope of $n = \hbar q^2/(4e\mu_0 H^i_{c2,\perp}) - 1/2$, where we index the transitions into the $i = 1, 2, \ldots$ LLs at $\mu_0 H^i_{c2,\perp} = \mu_0 H_{c2} \cos\theta_i$ as half-integers $n = 1/2, 3/2, \ldots$ (Fig. 3a, inset top)[37]. From the slope of the index plot (equal to $\hbar q^2/4e$), we obtain $q = (1.31 \pm 0.08) \times 10^{-3}$ Å^{-1} at $T = 20$ mK, decreasing to $(0.48 \pm 0.03) \times 10^{-3}$ Å^{-1} at 460 mK. The measured q at 20 mK is of the same order as q expected from Zeeman splitting (Fig. 3b, top; Methods).

Similar to fermionic QOs, oscillations of H_{c2} in the finite-q state could provide a powerful link between theoretical and experimental measures of the superconducting order. For example, studying oscillations of H_{c2} with in-plane rotation of H could probe deviations from $\mathcal{A}_q = \pi q^2$ due to in-plane anisotropy[25]. The spatial structure of $|\psi|^2$ in the field-induced state is also expected to change between different n: in the isotropic 2D limit, the $n = 0$ Abrikosov lattice gives way to stripe-like patterns for $n = 1$ and $n = 3$ interrupted by a triangular phase at $n = 2$ (Fig. 3a inset, bottom, Methods)[12,13,36]. Moreover, the local D_3 symmetry of the superconducting layers[28] could support finite-q phase modulations as soon as $H_\perp \ll H_\parallel \neq 0$, where $H_\parallel$ is the H component parallel to the a–b plane (ref. [38]; Methods). The van der Waals (vdW) superlattice construction of $Ba_6Nb_{11}S_{28}$ may permit real- and momentum-space imaging with small-angle neutron scattering[17], scanning tunnelling microscopy[18] or Josephson interferometry using vdW devices[19] to study these unusual structures.

Fermionic LLs in the normal state

We next turn to the fermionic LLs in $Ba_6Nb_{11}S_{28}$. Although Onsager's rule has proven invaluable in mapping $\mathcal{A}_k$ of metals, it was realized only recently that γ can be used to probe the electronic structure's topology[39]. Specifically, $\gamma = 1/2 - \varphi_B/2\pi$, where φ_B is the Berry phase, which is quantized to π (0) for topologically non-trivial (trivial) FSs. We map the fermiology of $Ba_6Nb_{11}S_{28}$ using de Haas–van Alphen (dHvA) QOs to examine γ. Figure 4a shows the field dependence of torque $\tau(H)$ at $T = 20$ mK and $\theta = 18.2°$ where QOs periodic in $1/H$ with frequencies $f = \hbar\mathcal{A}_k/2\pi e$ (ref. [37]) are seen for $\mu_0 H \gtrsim 1$ T. In addition to the large FSs sourcing superconductivity (fast oscillations at $\mu_0 H > 10$ T, Γ_1 and Γ_2 in Fig. 4e)[28], there are smaller FSs with closely spaced f's evidenced by interference nodes (Fig. 4a, black arrows). The fast Fourier transform (FFT) of $\tau(1/H)$ after removing a quadratic background (Fig. 4a inset, bottom, Methods) shows contributions at $f_\delta = 5.9$ T, $f_{\alpha_1} = 43.0$ T and $f_{\alpha_2} = 54.7$ T. We also observe a weak contribution at $f_{\alpha^*} \approx (f_{\alpha_1} + f_{\alpha_2})/2 = 48.9$ T, suggesting that it stems from magnetic breakdown[40] between the α_1 and α_2 FSs.

To determine γ, we use $M_\tau^{osc}(H) \propto -\sin(2\pi(f/\mu_0 H - \gamma))$ where M_τ^{osc} is the QO component of M_τ (ref. [37]). The sign of γ is tied to that of M_τ^{osc} which is fixed by the presence of both the Meissner effect and dHvA QOs in $\tau(H)$ (Fig. 4a, top inset). We extract φ_B using the phase-shift function $K(f, \phi) = \mathrm{Im}(e^{i\phi}\mathcal{F}(M_\tau^{osc}(H)))$, where $\mathcal{F}$ denotes an FFT, which peaks at (f, φ) pairs contributing to $M_\tau^{osc}(H)$[41] (Methods). Figure 4b shows a contour plot of $K(f, \varphi_B)$ for M_τ^{osc} from $\tau(H)$ in Fig. 4a, which

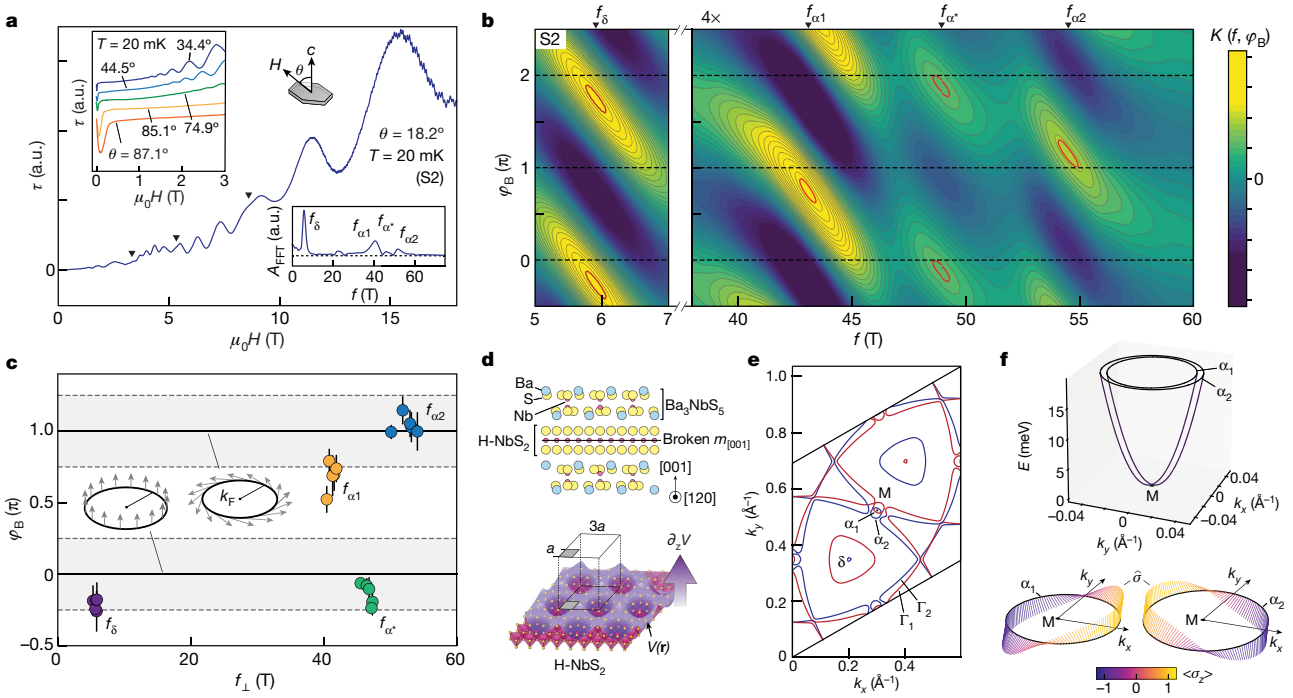

Fig. 4 | Berry phase of fermionic LLs. a, $\tau(H)$ at $T = 20$ mK for $\theta = 18.2°$ showing prominent dHvA QOs. Interference nodes are marked by arrows. Bottom inset, FFT of dHvA oscillations. Top inset, dHvA oscillations and the Meissner effect can be observed simultaneously (sample S2). **b**, Contour plots of the phase shift function $K(f, \varphi_B)$. Red contours are drawn where $K(f, \varphi_B)$ reaches 98% of its local maxima (sample S2). **c**, The (f, φ_B) composition of dHvA oscillations across five samples (samples S1–S5). The error bars of φ_B correspond to the range bounded by the 98% contours defined for **b**. Top inset, winding of a pseudospin-1/2 vector along the FS yields $\varphi_B = \pi$. Bottom inset, in the absence of this winding, $\varphi_B = 0$. **d**, Top, schematic cross-section of $Ba_6Nb_{11}S_{28}$ structure. Bottom, electronic structure can be modelled by imposing a mirror asymmetric, $3a$ periodic potential $V(r)$ onto the a periodic H-NbS_2 monolayer. **e**, Electronic structure from first principles. **f**, Top, electronic structure around the M point determined from dHvA oscillations with a band touching point at M apparent. The experimentally observed α_1 and α_2 orbits are drawn as black contours. Bottom, $\hat{\sigma}$ along α_1 and α_2 exhibit winding characteristic of $\varphi_B = \pi$. Colour corresponds to the σ_z component of spin.

yields $\varphi_B = (0.7 \pm 0.1)\pi$ and $(1.0 \pm 0.1)\pi$ ($(-0.1 \pm 0.1)\pi$ and $(-0.2 \pm 0.1)\pi$) for f_{α_1} and f_{α_2} (f_{α^*} and f_δ), respectively. Figure 4c summarizes φ_B versus $f_\perp$ across five samples, where $f_\perp = f\cos\theta$ accounts for variation of θ (< 5°) (Methods). Across these samples, comparable f_{α_1} and f_{α_2}, and magnetic breakdown f_{α^*} suggests that α_1 and α_2 form a two-band system; $\varphi_B = \pi$ signals 2π winding of their spin-1/2 eigenvector along the FSs (Fig. 4c, centre inset). Conversely, $\varphi_B = 0$ evidences no winding (Fig. 4c, left inset) and the f_δ pocket is consistent with this expectation (Methods).

These features of α_1 and α_2 recall bands with Rashba SOC in mirror asymmetric structures[42] such as quantum wells and interfaces. The mirror asymmetry in $Ba_6Nb_{11}S_{28}$ (Fig. 4d, top) and zone-folding due to the Ba_3NbS_5 layer (Fig. 4d, bottom) permit similar SOC, $H_{SOC} = \boldsymbol{\alpha}(\mathbf{k})\cdot\boldsymbol{\sigma}$ where $\boldsymbol{\alpha}(\mathbf{k})$ is an effective Zeeman field in momentum space ($\mathbf{k}$ space) and $\boldsymbol{\sigma}$ is the Pauli spin vector (Methods). Extracting $\boldsymbol{\alpha}$ from QOs, we compute the band structure around the M point with the α_1 and α_2 orbits shown as black contours (Figure 4f, top). Paralleling Rashba SOC, a linear band crossing at M and winding of the spin unit-vector $\hat{\boldsymbol{\sigma}}$ along the FSs are apparent (see Fig. 4f, bottom, colour maps to z component of spin σ_z).

The coexistence of Rashba-like FSs and bulk superconductivity is reminiscent of Fe(Se,Te)[43] and may connect to predictions for field-induced topological superconductivity[44]. Our analysis suggests that the hierarchy of energy scales for SOC, superconductivity and small interlayer coupling may be conducive for topological superconductivity at $H = 0$ (Methods). Coupled with signatures of finite-q pairing and bosonic LL transitions, this raises prospects of studying the interplay among these disparate phenomena. One of the few predictions at this intersection is an unusual arrangement of Majorana fermions localized to nodes in ψ (ref. [45]). The consequences of Cooper pairs in higher LLs and the topology of the electronic structure seems to be the least explored aspect. This material may provide the impetus to address these open questions.

Online content

Any methods, additional references, Nature Research reporting summaries, source data, extended data, supplementary information, acknowledgements, peer review information; details of author contributions and competing interests; and statements of data and code availability are available at https://doi.org/10.1038/s41586-021-03915-3.

1. Shoenberg, D. The de Haas–Van Alphen Effect. *Phil. Trans. R. Soc. A* **245**, 1–57 (1952).
2. Bartolomei, H. et al. Fractional statistics in anyon collisions. *Science* **368**, 173–177 (2020).
3. Nakamura, J., Liang, S., Gardner, G. C. & Manfra, M. J. Direct observation of anyonic braiding statistics. *Nat. Phys.* **16**, 931–936 (2020).
4. Cooper, N. R., Wilkin, N. K. & Gunn, J. M. F. Quantum phases of vortices in rotating Bose–Einstein condensates. *Phys. Rev. Lett.* **87**, 120405 (2001).
5. Senthil, T. & Levin, M. Integer quantum Hall effect for bosons. *Phys. Rev. Lett.* **110**, 046801 (2013).
6. Schine, N., Ryou, A., Gromov, A., Sommer, A. & Simon, J. Synthetic Landau levels for photons. *Nature* **534**, 671–675 (2016).
7. Fletcher, R. J. et al. Geometric squeezing into the lowest Landau level. *Science* **372**, 1318–1322 (2021).
8. Fulde, P. & Ferrell, R. A. Superconductivity in a strong spin-exchange field. *Phys. Rev.* **135**, A550–A563 (1964).
9. Larkin, A. I. & Ovchinnikov, Y. I. Inhomogeneous state of superconductors. *Sov. Phys. JETP* **20**, 762–769 (1965).
10. Bulaevskii, L. N. Inhomogeneous state and the anisotropy of the upper critical field in layered superconductors with Josephson layer interaction. *Sov. Phys. JETP* **38**, 634–639 (1974).
11. Shimahara, H. & Rainer, D. Crossover from vortex states to the Fulde–Ferrell–Larkin–Ovchinnikov state in two-dimensional s- and d-wave superconductors. *J. Phys. Soc. Jpn* **66**, 3591–3599 (1997).

12. Klein, U. Two-dimensional superconductor in a tilted magnetic field: states with finite Cooper-pair momentum. *Phys. Rev. B* **69**, 134518 (2004).
13. Yang, K. & MacDonald, A. H. Vortex-lattice structure of Fulde–Ferrell–Larkin–Ovchinnikov superconductors. *Phys. Rev. B* **70**, 094512 (2004).
14. Bulaevskii, L. N. Magnetic properties of layered superconductors with weak interaction between the layers. *Sov. Phys. JETP* **37**, 1133–1136 (1973).
15. Onsager, L. Interpretation of the de Haas–van Alphen effect. *Phil. Mag.* **43**, 1006–1008 (1952).
16. Kasahara, Y. et al. Majorana quantization and half-integer thermal quantum Hall effect in a Kitaev spin liquid. *Nature* **559**, 227–231 (2018).
17. Huxley, A. et al. Realignment of the flux-line lattice by a change in the symmetry of superconductivity in UPt_3. *Nature* **406**, 160–164 (2000).
18. Wang, D. et al. Evidence for Majorana bound states in an iron-based superconductor. *Science* **362**, 333–335 (2018).
19. Yang, K. & Agterberg, D. F. Josephson effect in Fulde–Ferrell–Larkin–Ovchinnikov superconductors. *Phys. Rev. Lett.* **84**, 4970–4973 (2000).
20. Wen, X.-G. Topological orders and edge excitations in fractional quantum Hall states. *Adv. Phys.* **44**, 405–473 (1995).
21. Lilly, M. P., Cooper, K. B., Eisenstein, J. P., Pfeiffer, L. N. & West, K. W. Evidence for an anisotropic state of two-dimensional electrons in high Landau levels. *Phys. Rev. Lett.* **82**, 394–397 (1999).
22. Amet, F. et al. Supercurrent in the quantum Hall regime. *Science* **352**, 966–969 (2016).
23. Klemm, R. A. *Layered Superconductors* (Oxford Univ. Press, 2012).
24. Burkhardt, H. & Rainer, D. Fulde–Ferrell–Larkin–Ovchinnikov state in layered superconductors. *Ann. Phys.* **506**, 181–194 (1994).
25. Dao, V. H., Denisov, D., Buzdin, A. & Brison, J.-P. Role of crystal anisotropy on the vortex state in the Fulde–Ferrell–Larkin–Ovchinnikov (FFLO) phase. *Phys. Rev. B* **87**, 174509 (2013).
26. Matsuda, Y. & Shimahara, H. Fulde–Ferrell–Larkin–Ovchinnikov state in heavy fermion superconductors. *J. Phys. Soc. Jpn* **76**, 051005 (2007).
27. Wosnitza, J. FFLO states in layered organic superconductors. *Ann. Phys.* **530**, 1700282 (2018).
28. Devarakonda, A. et al. Clean 2D superconductivity in a bulk van der Waals superlattice. *Science* **370**, 231–236 (2020).
29. Tinkham, M. *Introduction to Superconductivity* (Dover Publications, 2004).
30. Gruenberg, L. W. & Gunther, L. Fulde–Ferrell effect in type-II superconductors. *Phys. Rev. Lett.* **16**, 996–998 (1966).
31. Klemm, R. A., Luther, A. & Beasley, M. R. Theory of the upper critical field in layered superconductors. *Phys. Rev. B* **12**, 877–891 (1975).
32. Lu, J. M. et al. Evidence for two-dimensional Ising superconductivity in gated MoS_2. *Science* **350**, 1353–1357 (2015).
33. Uji, S. et al. Quantum vortex melting and phase diagram in the layered organic superconductor κ-$(BEDT\text{-}TTF)_2Cu(NCS)_2$. *Phys. Rev. B* **97**, 024505 (2018).
34. Modler, R. "Anomalous peak effect"—Is it indicative of a generalized Fulde–Ferrell–Larkin–Ovchinnikov state? *Czech. J. Phys.* **46**, 3123–3130 (1996).
35. Kawamata, S., Itoh, N., Okuda, K., Mochiku, T. & Kadowaki, K. Observation of anisotropic pinning effect in $Bi_2Sr_2CaCu_2O_{8+\delta}$ single crystals. *Physica C* **195**, 103–108 (1992).
36. Abrikosov, A. A. Nobel Lecture: Type-II superconductors and the vortex lattice. *Rev. Mod. Phys.* **76**, 975–979 (2004).
37. Shoenberg, D. *Magnetic Oscillations in Metals* (Cambridge Univ. Press, 2009).
38. Smidman, M., Salamon, M. B., Yuan, H. Q. & Agterberg, D. F. Superconductivity and spin–orbit coupling in non-centrosymmetric materials: a review. *Rep. Prog. Phys.* **80**, 036501 (2017).
39. Mikitik, G. P. & Sharlai, Y. V. Manifestation of Berry's phase in metal physics. *Phys. Rev. Lett.* **82**, 2147–2150 (1999).
40. Falicov, L. M. & Sievert, P. R. Magnetoresistance and magnetic breakdown. *Phys. Rev. Lett.* **12**, 558–561 (1964).
41. Schneider, J. M., Piot, B. A., Sheikin, I. & Maude, D. K. Using the de Haas–van Alphen effect to map out the closed three-dimensional Fermi surface of natural graphite. *Phys. Rev. Lett.* **108**, 117401 (2012).
42. Manchon, A., Koo, H. C., Nitta, J., Frolov, S. M. & Duine, R. A. New perspectives for Rashba spin–orbit coupling. *Nat. Mater.* **14**, 871–882 (2015).
43. Zhang, P. et al. Observation of topological superconductivity on the surface of an iron-based superconductor. *Science* **360**, 182–186 (2018).
44. Potter, A. C. & Lee, P. A. Engineering a $p + ip$ superconductor: comparison of topological insulator and Rashba spin–orbit-coupled materials. *Phys. Rev. B* **83**, 184520 (2011).
45. Hu, L. H., Liu, C. X. & Zhang, F. C. Topological Larkin–Ovchinnikov phase and Majorana zero mode chain in bilayer superconducting topological insulator films. *Commun. Phys.* **2**, 25 (2019).

Methods

Cantilever torque magnetometry

We use torque magnetometry to examine the magnetization response of $Ba_6Nb_{11}S_{28}$. For $H_{\parallel} \equiv H\sin\theta \neq 0$, where θ is measured relative to the c axis, a torque $\tau = M \times \mu_0 H$ parallel to the a–b plane is experienced by the material (Extended Data Fig. 1a). Owing to the suppression of interlayer coupling in this material, screening supercurrents are largely confined to the a–b plane[46–48]; for θ near 90°, the M response is largely due to screening supercurrents and is predominantly oriented along the c axis. We probe M by mounting samples onto mechanical cantilevers and sensing their deflection owing to τ. Extended Data Fig. 1b, c shows representative capacitive (sample S1) and resistive (sample S2) torque magnetometers, respectively, used in this study. The capacitive torque magnetometer is constructed by mounting a $Ba_6Nb_{11}S_{28}$ crystal on a Cu:Be cantilever with dimensions 3 mm × 1.5 mm × 0.005 mm (length × width × thickness, $L \times W \times t$) and suspending it 250 μm over a gold-coated substrate. The resistive torque magnetometers are commercially available silicon cantilevers.

We sense deviations in capacitance $\delta C = C - C_0$ relative to the zero-field value C_0 using an Andeen–Hagerling 2500A or 2700A capacitance bridge. To measure deviation in resistance δR from τ for the resistive magnetometers, it is important to eliminate background contributions from magnetoresistance. We accomplish this by balancing piezoresistive elements with and without samples at zero field using a Wheatstone bridge. By exciting the bridge with voltage V_{ex}, we can sense δV, which is proportional to δR. In the linear response regime, δC (δR) is proportional to τ from which we can compute the torque magnetization $M_\tau \equiv \delta C/(\mu_0 H\sin\theta)$ ($M_\tau \equiv \delta V/(\mu_0 H\sin\theta)$), which is proportional to M. The δC maximum for capacitive cantilevers can be used to extract its maximum angular deflection $\delta\theta$. Specifically, $\delta\theta_{max} = \frac{d_0}{l}(\delta C_{max}/C_0)$ where d_0, l and C_0 are the initial cantilever-plate separation, length of the cantilever and zero-field capacitance, respectively. The typical $\delta C_{max} \approx 0.8$ fF (Extended Data Fig. 1d) and $C_0 \approx 0.27$ pF corresponds to $\delta\theta_{max} \leq 0.015°$. This indicates that the cantilever is within the linear response regime and, furthermore, enables the high-resolution angular dependence presented in the main text.

Extended Data Fig. 1e compares $M_\tau(T)$ measured with small $\mu_0 H_\perp = 0.4$ mT and resistivity $\rho_{xx}(T)$ for sample S1, demonstrating that the onset of diamagnetism and the zero-resistance state coincide at $T_c = 0.85$ K. Similarly, Extended Data Fig. 1f compares the up- and down-sweep $M_\tau(H)$ and $\rho_{xx}(H)$ at $T = 0.3$ K and $\theta = 89.7°$ for sample S1. The fact that $\rho_{xx}(H^\star) = 0$ shows that $\mu_0 H^\star$ marks a transition within the superconducting state. Furthermore, the upper critical field, defined throughout as the field where $M_\tau(H)$ is reduced to 5% of its peak at H_{c1}, is consistent with where ρ_{xx} becomes finite. We have checked that alternative methods of identifying H_{c2}, for example, using the irreversibility field (see, for example, ref. [49]) or by linear extrapolation of M_τ above $H^\star$ to zero, yield similar results.

Extended Data Fig. 1g shows $M(H)$ measured in a commercial superconducting quantum interference device (SQUID) magnetometer at $T = 0.4$ K at $\theta = 0°$. The system exhibits prominent diamagnetism from the Meissner effect, which gives way at higher fields to a mixed state indicative of type II superconductivity. The response is largely reversible, indicative of this system's cleanliness[50,51]. Extended Data Fig. 1h shows $\tau(H)$ and $M_\tau(H)$ loops measured at $T = 0.3$ K at $\theta = 46°$ (sample S1, inset and main panel, respectively) exhibiting similar behaviour to M measured by SQUID magnetometry.

We use a two-step process to precisely calibrate the sample angle relative to H. First, we calibrate the angle offset between the sample and a co-mounted Hall sensor using the angle dependence of QOs. Given the highly 2D electronic structure in this system, the QO frequencies F evolve as

$$F(\theta_H) = \frac{F_0}{\cos(\theta_H - \theta_0)} \quad (2)$$

where θ_H is the angle of the co-mounted Hall sensor measured relative to the applied field (fixed to the solenoid magnet axis), θ_0 is the sample offset angle relative to the Hall sensor and F_0 is the oscillation frequency at $\theta_H - \theta_0 = 0°$. We use the small δ oscillation (Fig. 4a) with $F_0 \approx 5$ T to perform the offset calibration as we can readily observe it at high angles $\theta_H \approx 80°$ (Extended Data Fig. 1i, orange points). For the example shown in Extended Data Fig. 1i for sample S1, the fit to the above equation yields $F_0 = 5.45 \pm 0.04$ T and $\theta_0 = -1.3° \pm 0.2°$. With this estimate of θ_0, we measured $M_\tau(H)$ at fine angular steps near $\theta_H - \theta_0 = 90°$. We further refine θ_0 by identifying the angle where $M_\tau(H)$ oscillates about zero (Extended Data Fig. 1i, inset). For sample S1, this yields $\theta_0 = -1.175°$ with precision equal to the angle step between data points. Comparable offsets are seen for the other samples.

Phase diagram of emergent superconducting state

In Fig. 2b, we present the phase diagram of the superconducting state at $\theta = 89.7°$. To find $H^\star$, we use the derivative $\partial M_\tau(H)/\partial H$ where the abrupt change in $M_\tau(H)$ appears as a peak-like structure for $T < T^\star = 0.44$ K. Extended Data Fig. 2a shows $\partial M_\tau(H)/\partial H$ (vertically offset for clarity) for the data shown in Fig. 2a where $H^\star$ is traced by a guide to the eye (grey dashed line). We also examine $M_\tau(H)$ and the phase diagram of the superconducting state in a wider angular window. Extended Data Fig. 2b shows a survey of $M_\tau(H)$ at $T = 0.31$ K (vertically offset for clarity) in the region $81.95° \leq \theta \leq 89.92°$. The kink-like feature and hysteresis between increasing (solid) and decreasing field (dashed) traces can be seen for $\theta \gtrsim 89.34°$. At lower angles, the traces are smooth and reversible. This is consistent with the two distinct field regimes identified by transport measurements on $Ba_6Nb_{11}S_{28}$ (ref. [28]). Extended Data Fig. 2c shows $M_\tau(H)$ for $\theta = 89.2°$ at multiple fixed temperatures. At all temperatures, $M_\tau(H)$ is smooth and reversible, unlike the behaviour at $\theta = 89.7°$ (Fig. 2a). Furthermore, the derivative $\partial M_\tau(H)/\partial H$ of the up-sweep traces (Extended Data Fig. 2d) does not show the peak-like structure marking $H^\star$. The phase diagram at this angle (Extended Data Fig. 2e) also reflects the absence of $H^\star$, marking the emergent superconducting state.

Extended Data Fig. 3a shows $M_\tau(H)$ for sample S2 at $\theta = 88.9°$ (vertically offset for clarity) at fixed T between 33 mK and 595 mK. Consistent with results for S1, the kink-like feature and hysteresis between up and down sweeps (Extended Data Fig. 3a, solid and dashed, respectively) appears for $T \lesssim 0.27$ K. This is further reinforced by $\partial M_\tau(H)/\partial H$ of the up-sweep traces (Extended Data Fig. 3b) where the peak-like structure characteristic of $H^\star$ is apparent for $T \lesssim 0.27$ K. A notable feature in $M_\tau(H)$ and its derivative (Extended Data Fig. 3a, b, respectively) is the jagged-structure for $\mu_0 H \lesssim 0.5$ T, which becomes increasingly prominent as T is lowered. The absence of this feature at higher T reflects similar phenomenology observed in other anisotropic SCs[52–55]. The phase diagram of the superconducting state at $\theta = 88.9°$ down to $T = 33$ mK is shown in Extended Data Fig. 3c, which is qualitatively similar to Fig. 2b.

The hysteresis observed in $M_\tau(H)$ points to metastability between the BCS and field-induced state separated by a first-order transition[56]. At $T = 20$ mK and $\theta = 89.7°$, the transitions at $H^\star$ and H' on increasing and decreasing H, respectively, demarcate this region of metastability (Fig. 2c). At higher T, this region of metastability appears washed out (Fig. 2a, b), consistent with the increased thermal energy available to overcome the energy barrier separating these states in the metastable region. This is also consistent with the fact that $\mu_0 H^\star(T = 0) = 1.28 \pm 0.05$ T extrapolated from the high-T 2D-GL fit (Fig. 2b) and falls between $\mu_0 H = 1.2$ T and $\mu_0 H^\star = 1.5$ T at $T = 20$ mK (Fig. 2c). The slight reduction of $\mu_0 H^\star(T = 0)$ relative to $\mu_0 H_p \approx 1.5$ T is probably due to orbital or multiband effects[28,57].

More broadly, non-monotonic behaviour of $M(H)$ can sometimes arise due to changes in vortex pinning. Known as the 'peak effect', marked by a characteristic peak in $M(H)$, it is commonly seen in disordered SCs near H_{c2} as the vortex lattice reconfigures to coincide with defects[58]. A related 'anomalous peak effect' is seen in some clean, heavy fermion SCs such as $CeRu_2$ and UPd_2Al_3 (ref. [34]) stemming from

the *f* electrons in these materials[59]. The cleanliness, evidenced by the prominent QOs (Fig. 4a), and the absence of *f* electrons in $Ba_6Nb_{11}S_{28}$ are inconsistent with these effects. In addition, the features observed here are not antisymmetric with respect to the *H* sweep direction as seen for the peak effect[58]. Further, vortex pinning in layered SCs is expected to depend on $H_\perp$, suggesting angular dependence of the form $1/\cos\theta$ (see, for example, $Bi_2Sr_2CaCu_2O_{8+\delta}$ (ref. [35])). The absence of a peak effect in $M(H)$ measured by SQUID magnetometry for $\theta = 0°$ (Extended Data Fig. 1g) and the appearance of the kink together with irreversibility in $M_\tau(H)$ only near $\theta \approx 90°$ further suggest that conventional vortex physics effects do not play a role.

$M_\tau(H)$ at fixed T and θ

Extended Data Fig. 4 shows $M_\tau(H)$ and $\partial M_\tau(H)/\partial H$ for various θ at $T > 0.31$ K (sample S1). Similar to the behaviour described in the main text, the kink-like feature and hysteresis between up and down sweeps (solid and dashed, respectively) in $M_\tau(H)$ at 395 mK (Extended Data Fig. 4a) and 460 mK (Extended Data Fig. 4c) become apparent for θ greater than a critical value near 90°. Examining $\partial M_\tau(H)/\partial H$ of the up-sweep traces taken at 395 mK (Extended Data Fig. 4b) and 460 mK (Extended Data Fig. 4d), we can see corrugation akin to that at 0.31 K (Fig. 2e). Here we see three and two local minima at 395 mK and 460 mK, respectively. We can pinpoint θ for these local minima by examining $H_{c2}(\theta)$ at these temperatures (see main text).

Extended Data Fig. 5a, b shows up- and down-sweep traces, respectively, of $M_\tau(H)$ (vertically offset for clarity) for various θ at $T = 20$ mK (sample S2). Here the kink-like feature is markedly sharper than at higher temperatures and on the down sweep, there is an additional local minimum in M_τ at H', traced by dashed guide to the eye in Extended Data Fig. 5b. Examining $\partial M_\tau(H)/\partial H$ of the up-sweep traces (Extended Data Fig. 5c), we can again identify H^* as a peak-like structure, traced by a dashed guide to the eye. Similar to sample S1, H^* here exhibits local minima as a function of θ. Here we identify three transitions at $\theta_1 = 88.667° \pm 0.02°$, $\theta_2 = 89.212° \pm 0.02°$ and $\theta_3 = 89.755° \pm 0.02°$. The angular dependence of up- and down-sweep $M_\tau(H)$ at $T = 20$ mK for a third sample S3 (Extended Data Fig. 5c, inset solid and dashed, respectively) exhibits similar behaviour. For S3, the kink-like feature in the up sweep appears at θ between 88.31° and 89.14°, consistent with θ_1 for S2 at the same temperature. The hysteresis between up and down sweeps also becomes increasingly prominent as $\theta \to 90°$.

Comparing Extended Data Fig. 5b, c, we observe that H' and H^* evolve together. Combined with the appearance of hysteresis between up and down sweeps, this points to a first-order phase transition within the superconducting state. A first-order transition is consistent with calculations and thermodynamic studies[60] of low-dimensional organic SCs, which are candidates to host finite-*q* pairing. As noted in the previous section, the sharp angular dependence is unlike that of vortex dynamics as seen in, for example, the cuprates[35,61–63]. Instead, this angular dependence is consistent with 2D finite-*q* pairing, which is predicted to host the bosonic LL structure reported in the main text[10–12].

A notable feature of layered SCs with *H* aligned near 90° is the vortex lock-in effect characterized by a flux confined between superconducting layers[23,29]. The lock-in state is possible when the flux is unable to enter the superconducting layers corresponding to $H\cos\theta < H_{c1,\perp}$ where $H_{c1,\perp}$ is the lower critical field at $\theta = 0°$. The well defined H_{c1} (Fig. 2d) indicates that any potential lock-in is not present in the mixed state up to 89.95°. The crossover angle θ_{lock} above which the flux is locked-in throughout the superconducting state is given by $H_{c2}(\theta_{lock})\cos\theta_{lock} \approx H_{c1,\perp}$. Using $\mu_0 H_{c1,\perp} \approx 1$ mT at 0.3 K, obtained from $\mu_0 H_{c1}(89.7°) \approx 0.12$ T at 0.3 K (Fig. 2b), we estimate $\theta_{lock} \approx 89.97°$ (Fig. 3a), comparable to estimates in layered organic SCs[64]. The confinement of the lock-in effect to such high angles, arising due to extrinsic factors such as flux pinning at the sample surface[64] or demagnetization effects[65], have hampered experimental studies of this phenomenon since its initial prediction[66].

Ginzburg–Landau model near H_{c2}

Here we present the GL model for the finite-*q* state and bosonic LL transitions therein. At *H* near H_{c2} applied in the *a*–*b* plane and *T* near T^* ($T^* \approx 0.56\ T_c$ in 2D), the GL free energy up to second order in the order parameter ψ takes the form[67,68]

$$\delta F \propto \alpha|\psi|^2 + \beta|\nabla\psi|^2 + \gamma|\nabla^2\psi|^2 + \mathcal{O}(\psi^4) \tag{3}$$

where α, β and γ are *H*- and *T*-dependent GL parameters. Crucially, $\beta \propto (T - T^*)/T^*$ is less than zero for $T < T^*$ and favours spatial modulations in ψ. As discussed for Fig. 1c, the system stands to gain δF_{Zeeman} from spin polarization of unpaired electrons at nodes in ψ and the overall ψ is determined by competition between this and the curvature energy $\propto |\nabla^2\psi|^2$.

The eigenfunctions of equation (3) are planewaves $\psi \propto e^{i\mathbf{q}\cdot\mathbf{r}}$ ($\mathbf{r}$ is a vector in the *x*–*y* plane). In a 2D isotropic system, this yields a wine-bottle-shaped potential in the q_x–q_y plane (Extended Data Fig. 6a) with an ensemble of planewave solutions which satisfy $|\mathbf{q}|^2 = q_0^2 = -\beta/(2\gamma)$ and reach the minimum free energy $\delta F_0 = -(\beta/4\gamma)|\psi|^2$ (Extended Data Fig. 6a). When the field is tilted away from the *a*–*b* plane, the finite component $H_\perp$ along the *c* axis drives orbital motion of Cooper pairs in the *a*–*b* plane, which is accounted for in δF by the transformation $\nabla \to \nabla - i\frac{2e}{\hbar}\mathbf{A}$ where $\mathbf{A}$ is the magnetic vector potential. The free energy of the *n*th LL is given by[69]

$$\delta F_n = (-\beta\lambda + \gamma\lambda^2)|\psi|^2 \tag{4}$$

with $\lambda = \frac{4e\mu_0 H_\perp}{\hbar}(n + \frac{1}{2})$ and the optimal LL satisfies

$$\delta F_n - \delta F_0 = \left(\frac{\beta^2}{4\gamma} - \beta\lambda + \gamma\lambda^2\right)|\psi|^2 = 0 \tag{5}$$

The solution to equation (5) is $\lambda = \beta/2\gamma$, which can be cast into a form recalling LL transitions[37]

$$\hbar\omega_c\left(n + \frac{1}{2}\right) - E_q = 0 \tag{6}$$

with the Cooper pair cyclotron frequency $\omega_c = e\mu_0 H_\perp/m^*$ and kinetic energy $E_q = \hbar^2 q_0^2/4m^*$. Intuitively, the transition from planewave to LL solutions when $H_\perp \neq 0$ corresponds to a transition from continuous eigenvalues *q* to discrete eigenvalues labelled by *n*. This is depicted schematically by a radial cut of δF in Extended Data Fig. 6b that is continuous as a function of *q* (black line) for $H_\perp = 0$ and discretized at $\sqrt{(2n+1)/\ell_\perp^2}$ for $H_\perp \neq 0$ with the Cooper pair magnetic length $\ell_\perp = \sqrt{\hbar/(2e\mu_0 H_\perp)}$ where we have used the fact that $B \approx \mu_0 H$ near H_{c2} where *M* is vanishing. Paralleling 2D fermionic systems[37,70], transitions between LLs are marked by non-monotonic variation of δF, which is imprinted on H_{c2} (refs. [12,13]). Following the convention of fermionic systems, the transition points, which appear between LLs, are indexed to half-integer values of *n*. Rearranging equation (6), we arrive at the relation

$$2\pi(n + 1/2) = (\pi q_0^2)\ell_\perp^2, \tag{7}$$

which is the Cooper pair counterpart to Onsager's rule for fermionic systems (equation (1)), where the term πq_0^2 is the *q*-space area enclosed by a circle of radius q_0 (Extended Data Fig. 6a).

In general, in-plane anisotropy permits second-order cross-terms of the form $|\nabla_x\nabla_y\psi|^2$ to equation (3). Although the underlying eigenfunctions are still LLs, $\delta F_n - \delta F_0$ is now minimized by solutions with mixed *n* and the degree of mixing increases with anisotropy. In three-dimensional systems or layered systems with sizeable interlayer coupling $t_\perp$, the additional term $|\nabla_z^2\psi|^2$ supports modulation of ψ parallel to *H* in addition to LLs perpendicular to *H* (ref. [71]). Anisotropic order parameters can also introduce corrections[72]. These forms of

anisotropy can smear out modulations in $\delta F_n - \delta F_0$ and, correspondingly, H_{c2} (ref. [25]). The sharp features observed in the present system suggest that these anisotropy terms are weak. This is further supported by the good agreement between the observed transitions and the 2D isotropic index analysis (Fig. 3a, top inset, equation (7)).

The non-centrosymmetric local D_3 symmetry about the H-NbS_2 layers in $Ba_6Nb_{11}S_{28}$ supports an additional term in free energy[38]

$$\delta F_{NCS} = \kappa[H_x\psi^*(\nabla_x\psi) + H_y\psi^*(\nabla_y\psi) + \text{c.c.}] \quad (8)$$

where c.c. is the complex conjugate of the first two terms and κ is proportional to the relative difference in density of states $\delta n = (n_+ - n_-)/(n_+ + n_-)$ between the spin-up (n_+) and spin-down (n_-) FSs formed by SOC. Theory suggests a field-induced first-order phase transition into a finite-q state resembling the conventional FFLO phase diagram should persist for $\delta n \lesssim 0.25$ (refs. [73,74]). First-principles calculations show $\delta n \approx 0.11$ between the Γ_1 and Γ_2 pockets sourcing superconductivity[28] (see below and Fig. 4e), consistent with the conventional form of the first-order phase boundary seen here (Fig. 2b). Notably, $\delta n \neq 0$ suggests a phase modulation of $\psi \propto e^{i\mathbf{q}\cdot\mathbf{r}}$ should appear once $H_\perp \ll H_\parallel \neq 0$. Josephson interferometry techniques, possibly facilitated by the vdW construction of this material[19], could probe this additional unconventional phase.

In conventional metals, QOs become apparent once $\omega_c\tau \approx 1$, where τ is the electron scattering time. Spatially, this condition is equivalent to electrons maintaining phase coherence over the extent of their cyclotron orbit. In the context of Cooper pairs, we can compare their coherence length $\xi_0 = 0.18\frac{\hbar v_F}{k_B T_c}$, where k_B and v_F are the Boltzmann constant and the Fermi velocity, respectively, to $\ell_\perp$ and expect to resolve oscillations in H_{c2} when $\xi_0/\ell_\perp \approx 1$. For $Ba_6Nb_{11}S_{28}$ with $\xi_0 \approx 250$ nm (ref. [28]), this yields an onset field for oscillations $\mu_0 H_{\perp,on} \approx 5$ mT, which is consistent with $\mu_0 H_{\perp,on} \approx 3$ mT observed in the experiment (Fig. 3a, inset).

Estimating q

Near the Pauli-limit H_P, the Zeeman splitting Δ_{Zeeman} (Extended Data Fig. 6d) of the underlying bands that undergo Cooper pairing becomes comparable to the superconducting gap Δ_{SC} (Extended Data Fig. 6c, d). Schematically, formation of Cooper pairs between the Zeeman split spin-up and spin-down bands (Extended Data Fig. 6d) acquire finite q with $q \approx \Delta_{Zeeman} \times \partial k(E_F)/\partial E$. For isotropic bands, this is given by $q \approx (g\mu_B\mu_0 H)/\hbar v_F$, where g is the g-factor, μ_B is the Bohr magneton and v_F is the Fermi velocity. For the large Γ pockets, which have the largest density of states and are the likely origin of superconductivity[28], $v_F \approx 10^5$ m s^{-1} as determined from QOs. Near $\mu_0 H_{c2} \approx 2$ T, assuming $g = 2$, $q \approx 4 \times 10^{-4}$ Å^{-1}. This is the same order of magnitude as that obtained from the LL index analysis in the main text (Fig. 3c), again pointing to the Γ pockets as the likely source of finite-q pairing. Analogous to fermionic QOs, the LL index analysis is sensitive to $\mathcal{A}_q$ and our estimate of q assumes an isotropic contour in q space (see above). This suggests that examining corrugations in H_{c2} at different field-angle orientations may permit a detailed mapping of $\mathcal{A}_q$. This information may shed further light on the origins of finite-q pairing evidenced here.

Higher-index LL vortex lattice solutions

Analogous to conventional SCs[36], the lowest-order terms in the GL free energy (equation (3)) determine the eigenfunctions of ψ and the spatial structure of the vortex lattice is determined by higher-order terms. In the finite-q regime of a 2D SC, these take the form[12,13,67,68]

$$\delta F' \propto \epsilon|\psi|^4 + \zeta|\psi|^2|\nabla\psi|^2 + \eta[(\psi^*)^2(\nabla\psi)^2 + (\psi)^2(\nabla\psi^*)^2] + \nu|\psi|^6 \quad (9)$$

Using techniques employed to study fermionic LLs, Yang and MacDonald[13] developed a numerical technique to compute the optimal vortex lattice for arbitrary n parameterized by the reciprocal lattice vectors $\{\mathbf{g}_1, \mathbf{g}_2\}$. Given these reciprocal lattice vectors, tabulated in ref. [13], the spatial structure of $|\psi|^2$ has a closed form

$$|\psi(\mathbf{r})|^2 = \frac{1}{2\pi\ell_\perp^2}\sum_{m_1,m_2}(-1)^{m_1 m_2}\quad e^{-|m_1\mathbf{g}_1+m_2\mathbf{g}_2|^2\ell_\perp^2/4} \\ L_n\left(\frac{|m_1\mathbf{g}_1+m_2\mathbf{g}_2|^2\ell_\perp^2}{2}\right)\times\cos((m_1\mathbf{g}_1+m_2\mathbf{g}_2)\cdot\mathbf{r}) \quad (10)$$

where n is the LL index, L_n is the nth Laguerre polynomial, and m_1 and m_2 are integers. Given the Gaussian suppression factor $e^{-|m_1\mathbf{g}_1+m_2\mathbf{g}_2|^2\ell_\perp^2/4}$, contributions from large reciprocal lattice vectors are small and a numerical summation over a finite set of m_1 and m_2 captures the spatial structure. For the $|\psi|^2$ maps shown in Fig. 3, we sum over integers $m_1, m_2 \in [-50, 50]$.

Electronic structure from first-principles calculations

For the electronic structure modelling, we employed first-principles density functional theory calculations implemented in the Vienna Ab initio Simulation Package[75,76], based on the projector augmented wave[77] pseudopotential formalism and the Perdew–Burke–Ernzerhof[78] parameterized exchange-correlation energy functional. The electronic structure with and without SOC terms are converged with an energy cut-off of 310 eV and a Γ-centred $9 \times 9 \times 5$ Monkhorst–Pack k-mesh grid[79]. From the converged results, we derived an effective Wannier tight-binding model for the NbS_2 layer using the Wannier90 code[80–82]. We use Nb d_{z^2}, d_{xy} and $d_{x^2-y^2}$ orbitals in monolayer H-NbS_2 for the basis projection and find that this captures the relevant electronic degrees of freedom[83]. Starting with the monolayer electronic structure is supported by comparison with a bilayer model, where we find an interlayer coupling $t_\perp \approx 1$ meV compared with $t_\perp \approx 100$ meV in bulk transition metal dichalcogenides[84]. This signals the decoupling due to the spacer layers. This observation is also consistent with the high degree of two-dimensionality evidenced by QOs[28] (see below).

Schematically, as noted in the main text, the electronic structure of $Ba_6Nb_{11}S_{28}$ can be understood by starting with that of monolayer H-NbS_2 (Extended Data Fig. 7a), and zone-folding into a 3×3 smaller supercell Brillouin zone (sBZ, white lines in Extended Data Fig. 7a). The close approach of the H-NbS_2 FSs to M in the sBZ (Extended Data Fig. 7a, blue open circles) suggests that small pockets centred at this high-symmetry point will appear upon zone-folding. The results of folding are shown in Extended Data Fig. 7b. By imposing the potential due to the spacer layer, we obtain the electronic structure shown in Extended Data Fig. 7c. Consistent with earlier results[28], the electronic structure within about 10 meV of charge neutrality agree with QOs. An important consequence of zone-folding is the reduced role of Ising SOC, which otherwise strongly aligns spin along the z axis and yields unconventional behaviour of H_{c2} (refs. [32,85,86]). In monolayer H-NbS_2, the pockets exhibiting Ising SOC centred at $\overline{K}$ and $\overline{K}'$ are comparable in size to the pocket at $\overline{\Gamma}$ (Extended Data Fig. 7a). Upon zone-folding into the sBZ, we see that the Ising pockets at K and K′ are much smaller whereas the pocket centred at Γ is left relatively unaffected (Extended Data Fig. 7b, c).

We identify the smallest δ pockets at K and K′ (Extended Data Fig. 7d) as f_δ observed in QOs and the similarly sized α_1 and α_2 pockets at the M point (Extended Data Fig. 7e) as the closely spaced f_{α_1} and f_{α_2}. This identification is further supported by comparing the experimentally determined Berry phase φ_B and the calculated spin texture of these features. As noted in the main text, the presence (absence) of spin winding on the Bloch sphere is indicative of $\varphi_B = \pi$ ($\varphi_B = 0$) (see below)[87]. As seen in Extended Data Fig. 7f, the spin texture on the δ pocket is strongly aligned to the $+z$ axis. For clockwise motion around this pocket (Extended Data Fig. 7d, white arrow), the spin-texture precesses around the z axis of the Bloch sphere (Extended Data Fig. 7f, blue arrow). This strong alignment along the z axis is characteristic of Ising SOC and is consistent with the experimentally determined $\varphi_B \approx 0$ for f_δ (Fig. 4c). In contrast, the spin texture along the α_1 and α_2 pockets at M wind on the Bloch sphere (Extended Data Fig. 7g blue and red, respectively), consistent with $\varphi_B \approx \pi$ for f_{α_1} and f_{α_2} (Fig. 4c). This spin-texture winding

is captured in the symmetry derived **k**·**p** model, equation (11) (see below). We also confirm the quantized $\varphi_B = \pi$ using a numerical Wilson loop method[88].

M-point k·p model

Here we generate a **k**·**p** model near the M point using the crystal symmetry of $Ba_6Nb_{11}S_{28}$. The placement of *H*-NbS_2 monolayers between Ba_3NbS_5 spacer layers in $Ba_6Nb_{11}S_{28}$ leads to a symmetry reduction from their original point group $\bar{6}m2$ (D_{3h}) to the mirror asymmetric 32 (D_3) (see ref. [28]). As a result, the M point possess only time-reversal symmetry and two-fold rotation symmetry about the k_y axis (C_{2y}) as shown in Extended Data Fig. 7h[89–91].

We start from a SOC Hamiltonian of the form $H_{SOC} = \sum_{i=x,y,z} \sum_{j=x,y,z} \alpha_{ij}\sigma_i k_j$ where α_{ij} are the SOC coefficients, σ_i are the Pauli spin matrices and k_j are the momentum directions defined in Extended Data Fig. 7h. Working in two dimensions, we enforce $\alpha_{iz} = 0$ and use the action of C_{2y} on spin and crystal momentum to further restrict the H_{SOC}. Specifically, the action of C_{2y} takes $\langle k_x, k_y, k_z\rangle \to \langle -k_x, k_y, -k_z\rangle$ and $\langle \sigma_x, \sigma_y, \sigma_z\rangle \to \langle -\sigma_x, \sigma_y, -\sigma_z\rangle$ permitting non-zero values of only α_{xx}, α_{yy} and α_{zx}. Including the dispersion of the bands without SOC, we obtain the M-point Hamiltonian

$$H_M = \frac{\hbar^2 \mathbf{k}^2}{2m_0^\star} + \boldsymbol{\alpha}(\mathbf{k})\cdot\boldsymbol{\sigma} \tag{11}$$

with $m_0^\star$ the effective mass in the absence of SOC and $\boldsymbol{\alpha}(\mathbf{k}) = \langle \alpha_1 k_x, \alpha_2 k_y, \lambda k_x\rangle$ where we introduce the definitions $\alpha_1 \equiv \alpha_{xx}$, $\alpha_2 \equiv \alpha_{yy}$ and $\lambda \equiv \alpha_{zx}$. The vector $\boldsymbol{\alpha}(\mathbf{k})$ is equivalent to a **k**-dependent Zeeman field, yielding spin 1/2 eigenvectors $|\Psi_+\rangle$ and $|\Psi_-\rangle$ corresponding to $\boldsymbol{\alpha}(\mathbf{k})$ aligned and anti-aligned with $\boldsymbol{\alpha}(\mathbf{k})$, respectively. Their corresponding energies are

$$E_\pm = \frac{\hbar^2 k^2}{2m_0^\star} \pm \sqrt{(\alpha_1^2 + \lambda^2)k_x^2 + \alpha_2^2 k_y^2} \tag{12}$$

The SOC parameters can be obtained from the Wannier projected model by computing the matrix elements $\langle \Psi_\sigma | \frac{\partial H_W}{\partial k_i} | \Psi_{\sigma'}\rangle$ where H_W is Hamiltonian obtained from Wannier projection, $i = x, y$, and $\sigma, \sigma' = \pm$. We obtain $\lambda = 0.39$ eV Å, $\alpha_1 = -0.01$ eV Å and $\alpha_2 = 0.05$ eV Å, in nominal agreement with the experimental estimates (see below).

The equivalence of $\boldsymbol{\alpha}(\mathbf{k})$ to a **k**-dependent Zeeman field permits a straightforward calculation of the Berry phase φ_B by integrating the Berry connection along the M point FS contours. Along a closed FS defined by the **k**·**p** model, the spin-1/2 eigenvector $|\Psi\rangle$ evolves such that it remains collinear with $\boldsymbol{\alpha}(\mathbf{k})$. As a result, $|\Psi\rangle$ parameterized by the polar and azimuthal angles θ and φ, respectively (Extended Data Fig. 7i, black arrow), traces a closed contour $\mathcal{C}$ that encircles the Bloch sphere. Here we choose a gauge such that the eigenvectors are single-valued everywhere except the north pole and take the form

$$|\Psi_-\rangle = \begin{bmatrix} \sin\frac{\theta}{2} \\ -\cos\frac{\theta}{2}e^{i\varphi} \end{bmatrix}, |\Psi_+\rangle = \begin{bmatrix} \cos\frac{\theta}{2} \\ \sin\frac{\theta}{2}e^{i\varphi} \end{bmatrix} \tag{13}$$

Given that α_1, α_2 and λ are non-zero (see above), the eigenvectors are always single-valued. Furthermore, since M is a time-reversal invariant momentum, $\mathcal{C}$ can be split into two time-reversal related segments, $\mathcal{C}_a$ and $\mathcal{C}_b$ (Extended Data Fig. 7i, red and blue, respectively) such that $\mathcal{C} = \mathcal{C}_a + \mathcal{C}_b$. These two segments are related by the transformations $\theta \to \pi - \theta$ and $\varphi \to \pi + \varphi$. Focusing on $\mathcal{C}_a$, the Berry connection contribution from a small section of $\mathcal{C}_a$ is $\sin^2(\theta/2)\mathrm{d}\varphi$ (ref. [87]). The contribution from the time-reversed segment on $\mathcal{C}_b$ can be obtained by the above transformations of θ and φ, yielding $\cos^2(\theta/2)\mathrm{d}\varphi$. Integrating these contributions along $\mathcal{C}_a$ and $\mathcal{C}_b$ we find

$$\varphi_B = \int_{\mathcal{C}_a} \sin^2(\theta/2)\mathrm{d}\varphi + \int_{\mathcal{C}_b} \cos^2(\theta/2)\ \mathrm{d}\varphi = \int_0^\pi \mathrm{d}\varphi = \pi \tag{14}$$

The origin of $\varphi_B = \pi$ is non-zero α_1 and α_2 in equation (11), which are permitted by the broken *c* axis mirror symmetry (Fig. 4d). If this symmetry is reintroduced, which takes $\langle k_x, k_y, k_z\rangle \to \langle k_x, k_y, -k_z\rangle$ and $\langle \sigma_x, \sigma_y, \sigma_z\rangle \to \langle -\sigma_x, -\sigma_y, \sigma_z\rangle$, we find that α_1 and α_2 are disallowed while λ remains unrestricted. This is analogous to the origin of $\varphi_B = \pi$ in systems with Rashba SOC, for example, quantum wells, 2D electron gases confined to heterointerfaces, or polar bulk materials[42].

Finite magnetic field *H* acts to open a gap $\Delta_M = g\mu_B\mu_0 H$ at the M point. Whereas the Berry curvature Ω_B for $\Delta_M = 0$ is a δ function centred at M acting as a monopole source for φ_B, non-zero Δ_M acts to distribute Ω_B to **k** away from the M point, shown schematically in Extended Data Fig. 7j[87,92]. Consequently, φ_B, which is equal to integrating Ω_B in the finite area $\mathscr{A}_k$ enclosed by the FS contour (Extended Data Fig. 7j, black line), deviates by $\delta\varphi_B = \pi - \varphi_B$ from perfect quantization. For the **k**·**p** model considered here, $|\delta\varphi_B| \approx \pi\Delta_M/\sqrt{\Delta_M^2 + E_F^2}$, where E_F is the Fermi energy[93]. Assuming $g = 2$ and typical $\mu_0 H \approx 10$ T where we measure QOs, we find $\Delta_M \approx 1$ meV. With $E_F \approx 19$ meV (see below), we obtain $\delta\varphi_B \approx 0.1\pi$, which compares favourably with the deviations observed for the α pockets at the M point (Fig. 4c). The larger $\delta\varphi_B$ for α_1 relative to α_2 is consistent with the fact that its smaller $\mathcal{A}_k$ encloses less Ω_B, yielding a larger deviation from π. The observation of finite $\delta\varphi_B$ suggests a gap at M, which may be conducive to topological superconductivity.

de Haas–van Alphen oscillations

The oscillatory component of dHvA QOs is given by[37,94]

$$M_{osc} \propto -H^{1/2} \sum_i R_T^i R_D^i \sin(2\pi(f_i/\mu_0 H - \gamma_i)) \tag{15}$$

where R_T^i is the thermal damping factor, R_D^i is the Dingle factor, f_i is the oscillation frequency and γ_i is the phase shift, all of which are indexed by *i* which counts over the FS contours in the system.

Extended Data Fig. 8a shows the angular dependence of $M_\tau^{osc}(H_\perp)$, obtained from M_τ after subtracting a quadratic background (sample S1). The fact that $M_\tau^{osc}(H_\perp)$ is invariant for fixed θ spanning nearly 75° evidences the two-dimensionality of the electronic structure in this system. Extended Data Fig. 8b shows the temperature dependence of $M_\tau^{osc}(H)$ at $\theta = 18°$ for various fixed *T*. The suppression of the QO amplitude with increasing temperature is consistent with R_T^i and can be used to extract the effective mass.

We extract the amplitude from the FFT of M_τ^{osc} computed within a window of width H_w^{-1} centered on H_0^{-1}. The FFT amplitude normalized to its value at $T = 0.3$ K, $\widetilde{A}_{FFT}$, is shown in Extended Data Fig. 8c for the α_1, α_2 and δ oscillation frequencies. By fitting to R_T^i, we extract the effective mass for each pocket and obtain $m_\delta^\star = 0.11m_0$, $m_{\alpha_1}^\star = 0.34m_0$ and $m_{\alpha_2}^\star = 0.27m_0$, where m_0 is the free electron mass. The average effective mass for the α pocket is $0.31m_0$. From the oscillation frequencies, as discussed in the main text, we find $f_\delta = 5.9$T, $f_{\alpha_1} = 43.0$T and $f_{\alpha_2} = 54.7$T corresponding to $\mathcal{A}_k = 5.6 \times 10^{-4}$ Å^{-2}, 4.1×10^{-4} Å^{-2} and 5.2×10^{-3} Å^{-2}, respectively. The α_1 and α_2 frequencies and magnetic breakdown between them is captured by the **k**·**p** model (see below).

Magnetic breakdown

A magnetic field can induce tunnelling between distinct FS contours separated by relatively small energy gaps when the inverse magnetic length ℓ^{-1} becomes comparable to the momentum-space separation between FS contours[40,95]. This condition is satisfied at a characteristic breakdown field $\mu_0 H_{mb}$ and can be used to identify the momentum space separation δk between FS contours undergoing breakdown. Experimentally, magnetic breakdown is signalled by the emergence of new frequencies in QOs at $\mu_0 H_{mb}$ (ref. [96]). In addition, this emergent frequency has a simple algebraic relationship to the frequencies of the contours undergoing breakdown.

As discussed in the main text, $f_{\alpha^\star} \approx (f_{\alpha_1} + f_{\alpha_1})/2$ is suggestive of magnetic breakdown. To identify H_{mb} for $f_{\alpha^\star}$, we compute the FFT of M_τ^{osc} over a sliding window centered at H_0^{-1} with width H_w^{-1} (ref. [97]). Extended Data Fig. 8d shows the windowed (grey and orange) and un-windowed (blue) M_τ^{osc}, vertically offset for clarity, measured at $\theta = 8.2°$ and $T = 20$ mK. The windowing is performed for $(\mu_0 H_0)^{-1}$ equally spaced by 0.01 T^{-1} between 0.15 T^{-1} and 0.4 T^{-1} with $(\mu_0 H_w)^{-1} = 0.4$ T^{-1}. The corresponding FFT are shown in Extended Data Fig. 8e. We can see that the peak at $f_{\alpha^\star} = 48.9$ T is absent at higher H_0^{-1} where f_{α_1} and f_{α_2} are visible. Instead, it appears for $(\mu_0 H_0)^{-1} = 0.21$ T^{-1} (Extended Data Fig. 8d, e, orange) corresponding to $\mu_0 H_{mb} \approx 5$ T. The observed H_{mb} and its corresponding $\mathscr{E}_{mb}^{-1} \approx 0.01$ $Å^{-1}$ can be captured by the M point $\mathbf{k}\cdot\mathbf{p}$ model. This is further confirmed by a direct calculation of the FFT spectra and extraction of H_{mb} from the $\mathbf{k}\cdot\mathbf{p}$ model (see below).

Phase analysis

The phase shift γ_i of QOs in equation (15) can be a sensitive probe of the phase accumulated by an electron along its cyclotron orbit[39]. Specifically, $\gamma_i = 1/2 - \varphi_B/2\pi$, where the factor 1/2 is the Maslov term and φ_B is the Berry phase accumulated by the electron[98]. This has been utilized extensively to search for the $\varphi_B = \pi$ shift exhibited by bands with linear band crossings for example, in graphene[99] or surface states of topological insulators[100]. In such systems, the phase is often extracted using an LL index analysis where extrema or zero crossings in QOs are indexed and extrapolated to $(\mu_0 H)^{-1} = 0$ to obtain γ.

In multiband systems, this approach is faced with difficulties. In particular, identifying extrema or zero crossings proves challenging due to interference between multiple oscillations and in transport measurements, the sign of QOs may be difficult to identify[101]. Here the simultaneous observation of both the Meissner effect and dHvA QOs establishes the sign and removes this ambiguity (Extended Data Fig. 9a). To circumvent the issue of closely spaced frequencies, we employ the phase analysis technique developed to study dHvA QOs in graphite[41] where the phase-shift function $K(f, \varphi) = \mathrm{Im}[e^{i\varphi}\mathcal{F}(M_\tau^{osc}(H))]$, where $\mathcal{F}$ denotes an FFT, peaks at the (f_i, φ_i) contributions of equation (15).

Here we briefly illustrate the principle of this formalism. Focusing on the oscillatory component of equation (15), we can write it in the form $-\sin(2\pi(f_i/\mu_0 H - \gamma_i)) = \frac{i}{2}(e^{2\pi i(f_i/\mu_0 H - \gamma_i)} - e^{-2\pi i(f_i/\mu_0 H - \gamma_i)})$. Correspondingly, $\mathcal{F}[-\sin(2\pi(f_i/\mu_0 H - \gamma_i))] = \frac{i}{2}\{\delta(f - f_i)e^{-2\pi i\gamma_i} - \delta(f + f_i)e^{2\pi i\gamma_i}\}$ where $\delta(f)$ is the Dirac delta function in the frequency domain. The phase-shift function now takes the form

$$\begin{aligned} K(f, \varphi) &= \mathrm{Im}\left[\frac{i}{2}e^{i\varphi}(\delta(f - f_i)e^{-2\pi i\gamma_i} - \delta(f + f_i)e^{2\pi i\gamma_i})\right] \\ &= \frac{1}{2}\{\cos(\varphi - 2\pi\gamma_i)\delta(f - f_i) - \cos(\varphi + 2\pi\gamma_i)\delta(f + f_i)\} \end{aligned} \tag{16}$$

In real systems where the δ function is broadened due to R_T^i and R_D^i, $K(f, \varphi)$ peaks at $(f_i, 2\pi\gamma_i)$ and $(f_i, -2\pi\gamma_i)$. This can be used to compute the Berry phase for each frequency $\varphi_B^i = 2\pi(1/2 - \gamma_i)$.

Extended Data Fig. 9b shows $M_\tau^{osc}(1/H_\perp)$ measured at $T = 0.3$ K ($T = 20$ mK) for sample(s) S1 (S2–S5) at various angles near $\theta = 16°$. Given the two-dimensionality of the FSs (see above), all five samples can be treated on equal footing by using $H_\perp$. Extended Data Fig. 9c–f shows $K(f, \varphi_B)$ for f_δ (left panels) and f_α (right panel) for samples S1 and three additional samples S3, S4 and S5, respectively (S2 shown in Fig. 4b). The frequency and phase composition can be identified as peaks in the phase-shift function. Red contours are drawn where $K(f, \varphi_B)$ reaches 98% of its local maxima and are used to determine the uncertainty in φ_B (Fig. 4c).

k·p model fitting

Here we estimate $\mathbf{k}\cdot\mathbf{p}$ parameters using information from QOs. The dispersion for the inner (+) and outer (−) pockets at the M point is given by equation (12). As seen in the comparison to first-principles calculations, $\alpha_1 \ll \lambda$, which permits us to work with the two-parameter model

$$E_\pm = \frac{\hbar^2 k^2}{2m^\star} \pm \sqrt{\lambda^2 k_x^2 + \alpha_2^2 k_y^2} \tag{17}$$

For non-zero λ and α_2, the original, spin-degenerate circular FS contour with radius k_F^0 enclosing an area $\mathcal{A}_k = \pi(k_F^0)^2$ is split into two elliptical contours with semi-major and semi-minor axes $r_{maj} = k_F^0 \pm m_0^\star\hbar^2/\lambda$ and $r_{min} = k_F^0 \pm m_0^\star\hbar^2/\alpha_2$, where $m_0^\star$ is the average effective mass of the α_1 and α_2 pockets (see above), aligned along k_x and k_y, respectively.

The experimentally observed frequency difference between f_{α_1} and f_{α_2}, $\Delta f = f_{\alpha_2} - f_{\alpha_1}$, is related to the difference in area of the inner and outer FS contours through Onsager's rule. This yields $\Delta f \approx \frac{m_0^\star k_F^0}{\hbar e}(\lambda + \alpha_2)$, which constrains the total strength of the SOC terms. For the five samples examined here, we find $\Delta f = 11.7 \pm 0.7$ T (Extended Data Fig. 9) and $\lambda + \alpha_2 = 0.11 \pm 0.01$ eV Å. Given that λ is intrinsic to monolayer H-NbS_2 and α_2 originates from mirror symmetry breaking by the adjacent spacer layers, we further restrict ourselves to $\lambda > \alpha_2$. We find $\lambda \approx 0.07$ eV Å and $\alpha_2 \approx 0.04$ eV Å best match the observed oscillation frequencies f_{α_1} and f_{α_2}, the resulting FS contours shown in Extended Data Fig. 10a. The spin texture along the FSs obtained from these models is shown in Fig. 4f. We note that the value of α_2 obtained here is comparable to the strength of Rashba SOC in quantum wells and interfaces, for example, 0.04 eV Å in InGaAs/InAlAs (ref. [102]) and 0.05 eV Å on the surface of $SrTiO_3$ (ref. [103]).

Given this $\mathbf{k}\cdot\mathbf{p}$ model, we can compute the LL spectrum[104,105] and examine the behaviour of QOs. Extended Data Fig. 10b shows calculated QOs in the density of states assuming a Gaussian LL broadening of 0.2 meV corresponding to a scattering time $\tau \approx 3$ ps determined from the onset of QOs in experiment. The inset of Extended Data Fig. 10b shows the FFT power spectrum of the oscillations in the main panel where we can identify f_{α_1}, f_{α_2} and $f_{\alpha^\star}$ marked by red, blue and green arrows, respectively. By performing a windowed FFT analysis, we obtain the series of power spectra shown in Extended Data Fig. 10c, vertically offset for clarity, where we see that $f_{\alpha^\star}$ begins to develop at $\mu_0 H_{mb} \approx 6$ T, in agreement with experiment (see above). The ability to capture the observed frequencies, effective masses and magnetic breakdown demonstrates the power of the symmetry-based approach used to obtain the $\mathbf{k}\cdot\mathbf{p}$ model. This further suggests that substituting other transition metal dichalcogenides for H-NbS_2 in $Ba_6Nb_{11}S_{28}$ may yield a larger family of compounds exhibiting similar topological features in the electronic structure.

The parallels between this model and Rashba SOC suggests a bridge to topological superconductivity[44,106]. This, however, requires a detailed balance in the relevant energy scales of the system. Specifically, topologically non-trivial pairing can be stabilized when the Fermi energy E_F is located within an induced gap Δ_M at the M point, which satisfies $\Delta_M > \Delta_{SC}$ (ref. [44,106]). Recent theoretical work suggests that the interlayer coupling $t_\perp$ can introduce the necessary gap and host topological superconductivity[107]. First-principles calculations find $t_\perp \approx 1$ meV across the spacer layers, which would yield $\Delta_M = t_\perp$. The system then satisfies the required hierarchy of energy scales $\Delta_M > \Delta_{SC} = 1.764 k_B T_c \approx 0.13$ meV (assuming BCS pairing).

The application of an in-plane magnetic field would further increase Δ_M and, additionally, could realize coexisting finite-q and topological superconductivity. From the calculated LL spectrum (Extended Data Fig. 10d), we estimate $E_F \approx 19$ meV. This may be within the regime accessible by conventional gating techniques and given the exfoliable nature of this material (see the supplement of ref. [28]), a device structure may pave the way to realizing topological superconductivity in this system.

Data availability

The data presented in this article are available from the Harvard Dataverse at https://doi.org/10.7910/DVN/PLWWKA.

Code availability

The codes used for the density functional theory and analytical calculations in this study are available from the corresponding author upon reasonable request.

46. Wang, Y. et al. Field-enhanced diamagnetism in the pseudogap state of the cuprate $Bi_2Sr_2CaCu_2O_{8+\delta}$ superconductor in an intense magnetic field. *Phys. Rev. Lett.* **95**, 247002 (2005).
47. Bergemann, C. et al. Superconducting magnetization above the irreversibility line in $Tl_2Ba_2CuO_{6+\delta}$. *Phys. Rev. B* **57**, 14387–14396 (1998).
48. Li, L. et al. Diamagnetism and Cooper pairing above T_c in cuprates. *Phys. Rev. B* **81**, 054510 (2010).
49. Sugiura, S. et al. Fulde–Ferrell–Larkin–Ovchinnikov and vortex phases in a layered organic superconductor. *npj Quantum Mater.* **4**, 7 (2019).
50. Campbell, A. M., Evetts, J. E. & Dew-hughes, D. The behaviour of type II superconductors. *Phil. Mag.* **10**, 333–338 (1964).
51. Finnemore, D. K., Stromberg, T. F. & Swenson, C. A. Superconducting properties of high-purity niobium. *Phys. Rev.* **149**, 231–243 (1966).
52. Altshuler, E. & Johansen, T. H. Colloquium: Experiments in vortex avalanches. *Rev. Mod. Phys.* **76**, 471–487 (2004).
53. Swanson, A. G. et al. Flux jumps, critical fields, and de Haas–van Alphen effect in κ-$(BEDT\text{-}TTF)_2Cu(NCS)_2$. *Solid State Commun.* **73**, 353–356 (1990).
54. Tenya, K. et al. Anomalous pinning behavior in Sr_2RuO_4. *Physica B* **403**, 1101–1103 (2008).
55. Li, L., Checkelsky, J. G., Komiya, S., Ando, Y. & Ong, N. P. Low-temperature vortex liquid in $La_{2-x}Sr_xCuO_4$. *Nat. Phys.* **3**, 311–314 (2007).
56. Chaikin, P. M. & Lubensky, T. C. *Principles of Condensed Matter Physics* (Cambridge Univ. Press, 1995).
57. Takahashi, M., Mizushima, T. & Machida, K. Multiband effects on Fulde–Ferrell–Larkin–Ovchinnikov states of Pauli-limited superconductors. *Phys. Rev. B* **89**, 064505 (2014).
58. Campbell, A. M. & Evetts, J. E. Flux vortices and transport currents in type II superconductors. *Adv. Phys.* **21**, 199–428 (1972).
59. Roy, S. B. & Chaddah, P. Anomalous superconducting properties in $CeRu_2$: effects of magnetic and nonmagnetic substitutions. *Phys. Rev. B* **55**, 11100–11102 (1997).
60. Lortz, R. et al. Calorimetric evidence for a Fulde–Ferrell–Larkin–Ovchinnikov superconducting state in the layered organic superconductor κ-$(BEDT\text{-}TTF)_2Cu(NCS)_2$. *Phys. Rev. Lett.* **99**, 187002 (2007).
61. Farrell, D. E., Rice, J. P. & Ginsberg, D. M. Experimental evidence for flux-lattice melting. *Phys. Rev. Lett.* **67**, 1165–1168 (1991).
62. Beck, R. G., Farrell, D. E., Rice, J. P., Ginsberg, D. M. & Kogan, V. G. Melting of the Abrikosov flux lattice in anisotropic superconductors. *Phys. Rev. Lett.* **68**, 1594–1596 (1992).
63. Ooi, S., Shibauchi, T., Okuda, N. & Tamegai, T. Novel angular scaling of vortex phase transitions in $Bi_2Sr_2CaCu_2O_{8+y}$. *Phys. Rev. Lett.* **82**, 4308–4311 (1999).
64. Uji, S. et al. Orbital effect on FFLO phase and energy dissipation due to vortex dynamics in magnetic-field-induced superconductor λ-$(BETS)_2FeCl_4$. *J. Phys. Soc. Jpn* **82**, 034715 (2013).
65. Martínez, J. C. et al. Magnetic anisotropy of a $Bi_2Sr_2CaCu_2O_x$ single crystal. *Phys. Rev. Lett.* **69**, 2276–2279 (1992).
66. Feinberg, D. & Villard, C. Intrinsic pinning and lock-in transition of flux lines in layered type-II superconductors. *Phys. Rev. Lett.* **65**, 919–922 (1990).
67. Buzdin, A. I. & Kachkachi, H. Generalized Ginzburg–Landau theory for nonuniform FFLO superconductors. *Phys. Lett. A* **225**, 341–348 (1997).
68. Houzet, M. & Buzdin, A. Influence of the paramagnetic effect on the vortex lattice in 2D superconductors. *Europhys. Lett.* **50**, 375–381 (2000).
69. Denisov, D., Buzdin, A. & Shimahara, H. Types of Fulde–Ferrell–Larkin–Ovchinnikov states induced by anisotropy effects. *Phys. Rev. B* **79**, 064506 (2009).
70. Shoenberg, D. Magnetization of a two-dimensional electron gas. *J. Low Temp. Phys.* **56**, 417–440 (1984).
71. Yoshida, T., Sigrist, M. & Yanase, Y. Complex-stripe phases induced by staggered Rashba spin–orbit coupling. *J. Phys. Soc. Jpn* **82**, 074714 (2013).
72. Zhou, T. & Ting, C. S. Phase diagram and local tunneling spectroscopy of the Fulde–Ferrell–Larkin–Ovchinnikov states of a two-dimensional square-lattice *d*-wave superconductor. *Phys. Rev. B* **80**, 224515 (2009).
73. Yuan, N. F. Q. & Fu, L. Topological metals and finite-momentum superconductors. *Proc. Natl Acad. Sci. USA* **118**, e2019063118 (2021).
74. Agterberg, D. F. & Kaur, R. P. Magnetic-field-induced helical and stripe phases in Rashba superconductors. *Phys. Rev. B* **75**, 064511 (2007).
75. Kresse, G. & Furthmüller, J. Efficiency of ab-initio total energy calculations for metals and semiconductors using a plane-wave basis set. *Comput. Mater. Sci.* **6**, 15–50 (1996).
76. Kresse, G. & Furthmüller, J. Efficient iterative schemes for ab initio total-energy calculations using a plane-wave basis set. *Phys. Rev. B* **54**, 11169–11186 (1996).
77. Blöchl, P. E. Projector augmented-wave method. *Phys. Rev. B* **50**, 17953–17979 (1994).
78. Perdew, J. P., Burke, K. & Ernzerhof, M. Generalized gradient approximation made simple. *Phys. Rev. Lett.* **77**, 3865–3868 (1996).
79. Monkhorst, H. J. & Pack, J. D. Special points for Brillouin-zone integrations. *Phys. Rev. B* **13**, 5188–5192 (1976).
80. Marzari, N., Mostofi, A. A., Yates, J. R., Souza, I. & Vanderbilt, D. Maximally localized Wannier functions: theory and applications. *Rev. Mod. Phys.* **84**, 1419–1475 (2012).
81. Mostofi, A. A. et al. wannier90: a tool for obtaining maximally-localised Wannier functions. *Comput. Phys. Commun.* **178**, 685–699 (2008).
82. Mostofi, A. A. et al. An updated version of wannier90: a tool for obtaining maximally-localised Wannier functions. *Comput. Phys. Commun.* **185**, 2309–2310 (2014).
83. Liu, G.-B., Shan, W.-Y., Yao, Y., Yao, W. & Xiao, D. Three-band tight-binding model for monolayers of group-VIB transition metal dichalcogenides. *Phys. Rev. B* **88**, 085433 (2013).
84. Fang, S. et al. Ab initio tight-binding Hamiltonian for transition metal dichalcogenides. *Phys. Rev. B* **92**, 205108 (2015).
85. Xi, X. et al. Ising pairing in superconducting $NbSe_2$ atomic layers. *Nat. Phys.* **12**, 139–143 (2016).
86. Saito, Y. et al. Superconductivity protected by spin–valley locking in ion-gated MoS_2. *Nat. Phys.* **12**, 144–149 (2016).
87. Xiao, D., Chang, M. C. & Niu, Q. Berry phase effects on electronic properties. *Rev. Mod. Phys.* **82**, 1959–2007 (2010).
88. Fukui, T., Hatsugai, Y. & Suzuki, H. Chern numbers in discretized Brillouin zone: efficient method of computing (spin) Hall conductances. *J. Phys. Soc. Jpn* **74**, 1674–1677 (2005).
89. Aroyo, M. I. et al. Crystallography online: Bilbao Crystallographic Server. *Bulg. Chem. Commun.* **43**, 183–197 (2011).
90. Aroyo, M. I. et al. Bilbao Crystallographic Server: I. Databases and crystallographic computing programs. *Z. Kristallogr. Cryst. Mater.* **221**, 15–27 (2006).
91. Aroyo, M. I., Kirov, A., Capillas, C., Perez-Mato, J. M. & Wondratschek, H. Bilbao Crystallographic Server. II. Representations of crystallographic point groups and space groups. *Acta Crystallogr. A* **62**, 115–128 (2006).
92. Culcer, D., MacDonald, A. & Niu, Q. Anomalous Hall effect in paramagnetic two-dimensional systems. *Phys. Rev. B* **68**, 045327 (2003).
93. Wright, A. R. & McKenzie, R. H. Quantum oscillations and Berry's phase in topological insulator surface states with broken particle–hole symmetry. *Phys. Rev. B* **87**, 085411 (2013).
94. Alexandradinata, A., Wang, C., Duan, W. & Glazman, L. Revealing the topology of Fermi-surface wave functions from magnetic quantum oscillations. *Phys. Rev. X* **8**, 011027 (2018).
95. Kaganov, M. I. & Slutskin, A. A. Coherent magnetic breakdown. *Phys. Rep.* **98**, 189–271 (1983).
96. Harrison, N. et al. Magnetic breakdown and quantum interference in the quasi-two-dimensional superconductor κ-$(BEDT\text{-}TTF)_2Cu(NCS)_2$ in high magnetic fields. *J. Phys. Condens. Matter* **8**, 5415–5435 (1996).
97. Gvozdikov, V. M. & Taut, M. Magnetic quantum oscillations of electrons on a two-dimensional lattice: Numerical simulations and the magnetic breakdown approach. *Phys. Rev. B* **75**, 155436 (2007).
98. Fuchs, J. N., Piéchon, F., Goerbig, M. O. & Montambaux, G. Topological Berry phase and semiclassical quantization of cyclotron orbits for two dimensional electrons in coupled band models. *Eur. Phys. J. B* **77**, 351–362 (2010).
99. Zhang, Y., Tan, Y.-W., Stormer, H. L. & Kim, P. Experimental observation of the quantum Hall effect and Berry's phase in graphene. *Nature* **438**, 201–204 (2005).
100. Analytis, J. G. et al. Two-dimensional surface state in the quantum limit of a topological insulator. *Nat. Phys.* **6**, 960–964 (2010).
101. Xiong, J. et al. High-field Shubnikov–de Haas oscillations in the topological insulator Bi_2Te_2Se. *Phys. Rev. B* **86**, 045314 (2012).
102. Das, B. et al. Evidence for spin splitting in $In_xGa_{1-x}As/In_{0.52}Al_{0.48}As$ hetetorstructures as $B \rightarrow 0$. *Phys. Rev. B* **39**, 1411–1414 (1989).
103. Nakamura, H., Koga, T. & Kimura, T. Experimental evidence of cubic Rashba effect in an inversion-symmetric oxide. *Phys. Rev. Lett.* **108**, 206601 (2012).
104. Winkler, R. *Spin–Orbit Coupling Effects in Two-dimensional Electron and Hole Systems* (Springer, 2003).
105. Forsythe, C. et al. Band structure engineering of 2D materials using patterned dielectric superlattices. *Nat. Nanotechnol.* **13**, 566–571 (2018).
106. Alicea, J. Majorana fermions in a tunable semiconductor device. *Phys. Rev. B* **81**, 125318 (2010).
107. Nakosai, S., Tanaka, Y. & Nagaosa, N. Topological superconductivity in bilayer Rashba system. *Phys. Rev. Lett.* **108**, 147003 (2012).

Acknowledgements We are grateful to S. K. Yip, M. Shayegan and M. T. Randeria for discussions. This research is funded in part by the Gordon and Betty Moore Foundation through grant GBMF9070 to J.G.C. (instrumentation development), the Office of Naval Research (ONR) under award N00014-21-1-2591 (advanced characterization), the US Department of Energy (DOE) Office of Science, Basic Energy Sciences, under award DE-SC0019300 (material synthesis) and award DE-SC0022028 (structure analysis), the STC Center for Integrated Quantum Materials, NSF grant DMR-1231319 (E.K.) and the DOE Office of Basic Energy Sciences under award DE-SC0018945 (L.F.). S.F. acknowledges support from the Rutgers Center for Materials Theory Distinguished Postdoctoral Fellowship. Computations were performed on the Cannon cluster supported by the FAS Division of Science Research Computing Group (FASRC) at Harvard University. A portion of this work was performed at the National High Magnetic Field Laboratory, which is supported by NSF Cooperative Agreement DMR-1157490, the State of Florida, and DOE.

Author contributions A.D. and J.G.C. conceived the project. A.D. grew the single crystals, characterized the materials, and performed the measurements with T.S., J.Z., D.G. and M.K. supporting. A.D. performed the analytical calculations and S.F. and A.D. the electronic structure calculations with L.F. and E.K. supporting. A.D. and J.G.C. wrote the manuscript with contributions and discussions from all authors. J.G.C. supervised the project.

Competing interests The authors declare no competing interests.

Additional information

Supplementary information The online version contains supplementary material available at https://doi.org/10.1038/s41586-021-03915-3.

Correspondence and requests for materials should be addressed to J. G. Checkelsky.

Peer review information *Nature* thanks the anonymous reviewers for their contribution to the peer review of this work.

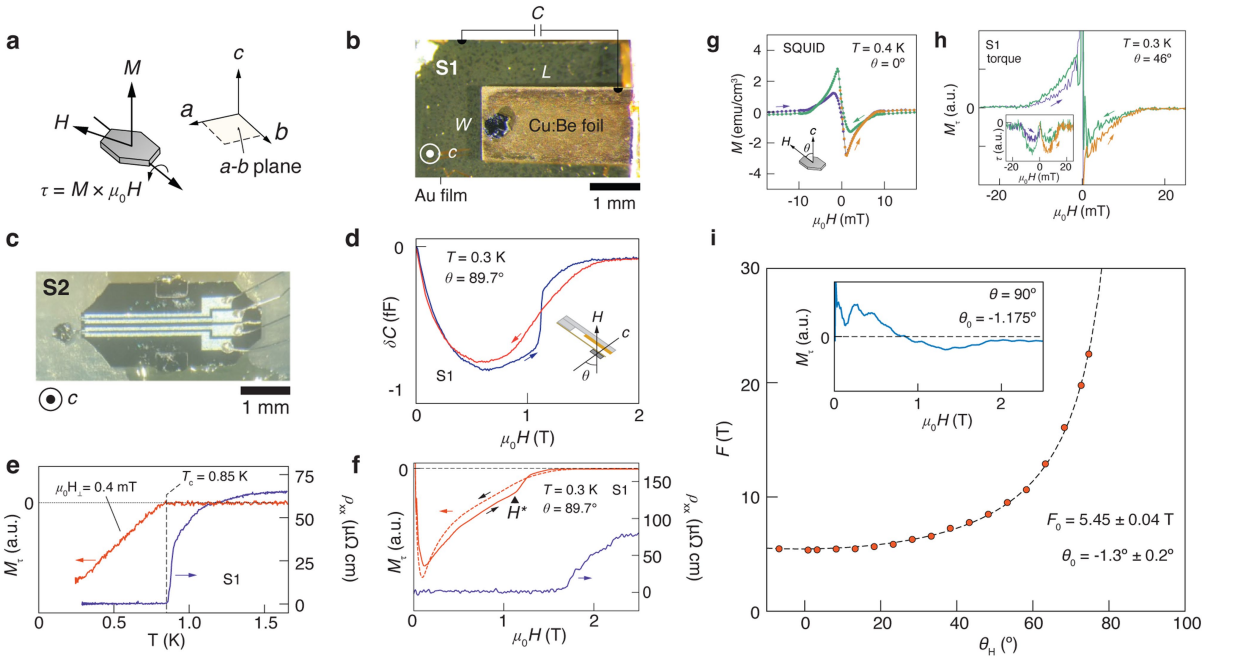

Extended Data Fig. 1 | Torque magnetometry. a Non-collinear response of M to H results in τ which can be measured using torque magnetometry techniques. **b** Capacitive torque magnetometer (sample S1). **c** Resistive torque magnetometer (sample S2). Scale bars are 1 mm. **d** $\delta C(H)$ at $\theta = 89.7°$ and $T = 0.3$ K for sample S1. (inset) The experimental geometry for S1. $\delta C < 0$ is consistent with diamagnetic response of M. **e** Comparison of $\rho_{xx}(T)$ and $M_\tau(T)$ measured with $\mu_0 H_\perp = 0.4$ mT for sample S1. **f** Comparison of $\rho_{xx}(H)$ and $M_\tau(H)$ at $\theta = 89.7°$ and $T = 0.3$ K for sample S1. **g** $M(H)$ loop for $\theta = 0°$ at $T = 0.4$ K measured by SQUID. **h** $M_\tau(H)$ loop for $\theta = 46°$ at $T = 0.3$ K measured by torque magnetometry (S1). (inset) $\tau(H)$ from which we obtain $M_\tau(H)$ in the main panel. **i** δ quantum oscillation frequency $F(\theta_H)$ (orange points) with fit to equation (2) (dashed line). (inset) θ where $M_\tau(H)$ oscillates around zero corresponds to $\theta = 90°$.

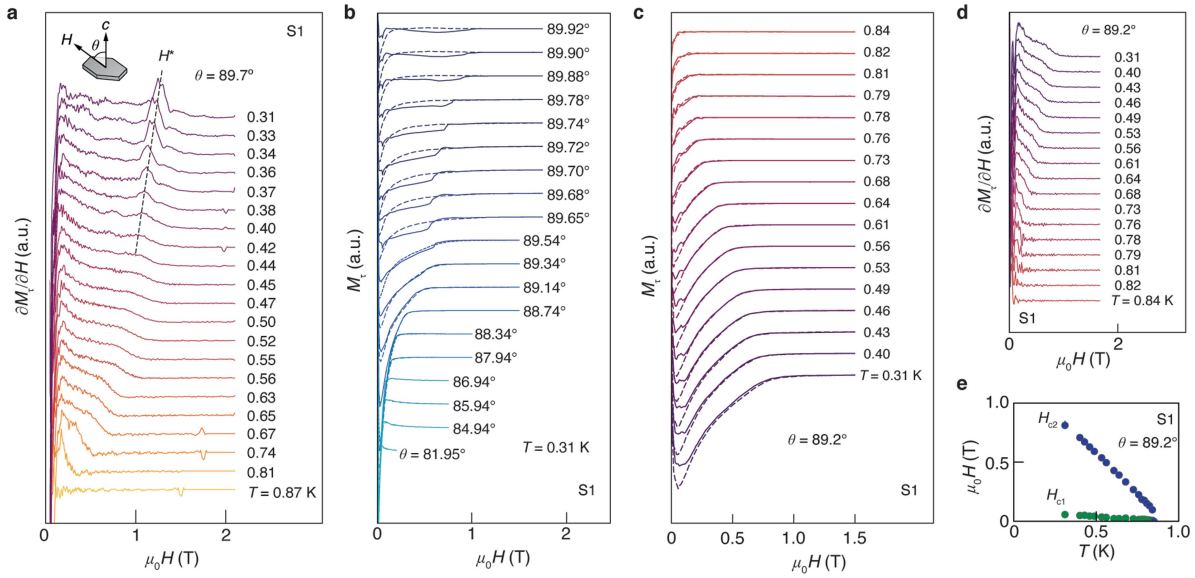

Extended Data Fig. 2 | Survey of *H*-*T*-*θ* phase space (sample S1). a $\partial M_\tau(H)/\partial H$ of up-sweep $M_\tau(H)$ (see Fig. 2a) at $\theta = 89.7°$ and various fixed temperatures, vertically offset for clarity. The peak-like structure marking H^* is traced by a dashed guide to the eye. **b** Up- (solid) and down-sweep (dashed) $M_\tau(H)$ measured at $T = 0.31$ K at various angles between 80° and 90°, vertically offset for clarity. **c** Up- (solid) and down-sweep (dashed) $M_\tau(H)$ measured at $\theta = 89.2°$ at various fixed temperatures, vertically offset for clarity. **d** $\partial M_\tau(H)/\partial H$ of up-sweep $M_\tau(H)$ at $\theta = 89.2°$ (shown in c) for various fixed temperatures, vertically offset for clarity. The peak-like structure marking H^* is absent here. **e** *T*-*H* phase diagram at $\theta = 89.2°$ showing H_{c2} and H_{c1}.

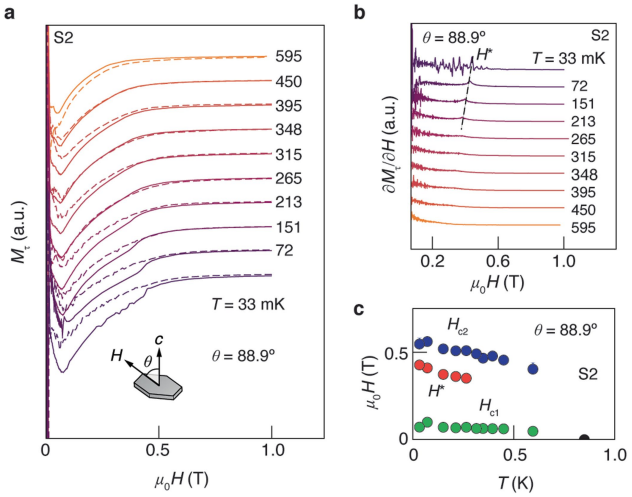

Extended Data Fig. 3 | *H*-*T* phase diagram (sample S2). a Up- (solid) and down-sweep (dashed) $M_\tau(H)$ measured at $\theta = 88.9°$ for various temperatures, vertically offset for clarity. **b** $\partial M_\tau(H)/\partial H$ of up-sweep $M_\tau(H)$ at $\theta = 88.9°$ (shown in a) for fixed temperatures down to $T = 33$ mK, vertically offset for clarity. The peak-like structure at H^* is traced by a dashed guide to the eye. **c** *T*-*H* phase diagram at $\theta = 88.9°$ showing H_{c2}, H^*, and H_{c1}. Black circle marks T_c.

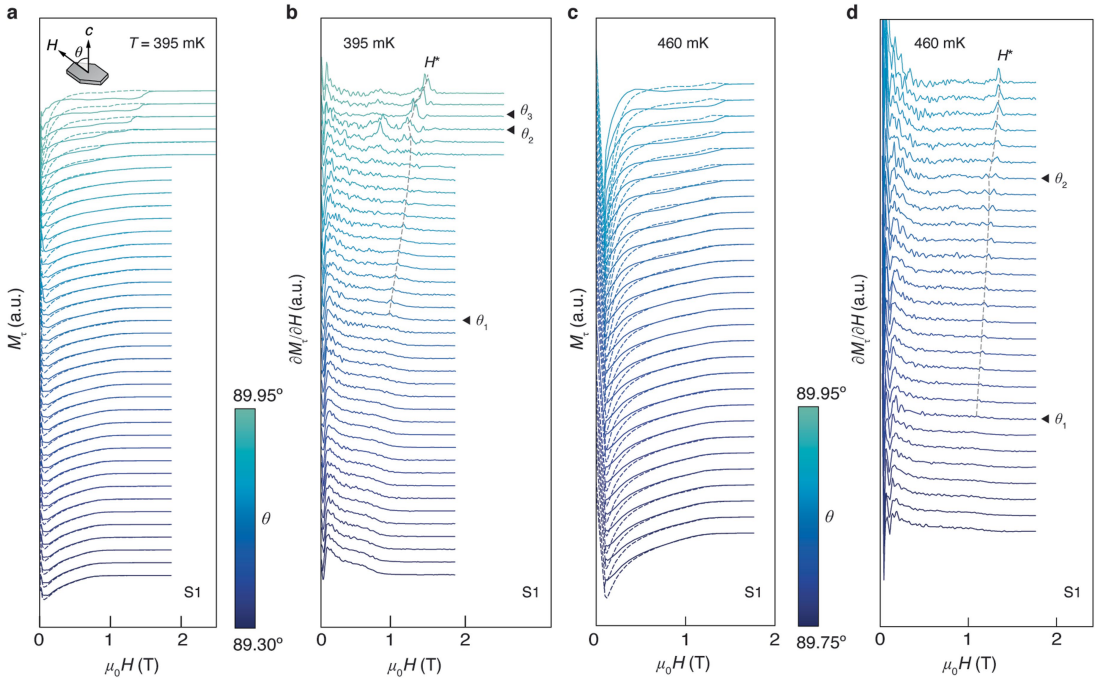

Extended Data Fig. 4 | $M_\tau(H)$ at fixed T and θ (sample S1). a Up- (solid) and down-sweeps (dashed) of $M_\tau(H)$ for $T = 395$ mK at equally spaced, fixed θ between 89.30° and 89.95°, vertically offset for clarity. **b** $\partial M_\tau(H)/\partial H$ of up-sweep in (a), vertically offset for clarity. Guide to the eye (grey dashed line) traces corrugation of $H^*(\theta)$. **c** Up- (solid) and down-sweeps (dashed) of $M_\tau(H)$ for $T = 460$ mK at equally spaced, fixed θ between 89.75° and 89.95°, vertically offset for clarity. **d** $\partial M_\tau(H)/\partial H$ of up-sweep in (c), vertically offset for clarity. Guide to the eye (grey dashed line) traces corrugation of $H^*(\theta)$.

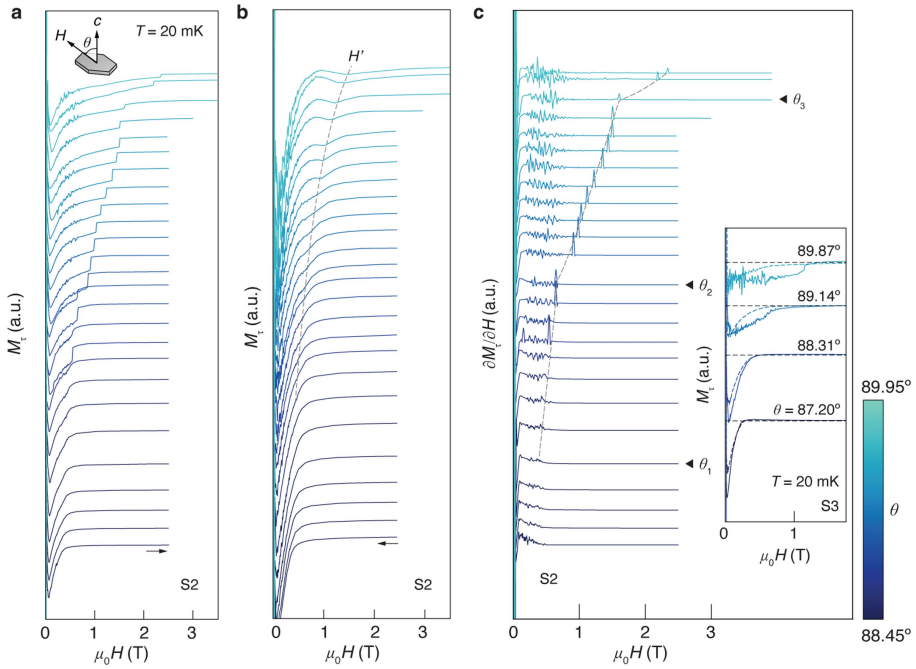

Extended Data Fig. 5 | Low temperature $M_\tau(H)$ at fixed θ. a Up- and **b** down-sweeps of $M_\tau(H)$ for $T = 20$ mK at equally spaced, fixed θ between 88.45° and 89.95°, vertically offset for clarity. Guide to the eye (grey dashed line) in (b) traces angular evolution of $H'(\theta)$ **c** $\partial M_\tau(H)/\partial H$ of up-sweep $M_\tau(H)$ in (a), vertically offset for clarity. Guide to the eye (grey dashed line) traces corrugation of $H^*(\theta)$ (inset) Up- and down-sweep $M_\tau(H)$ (solid and dashed, respectively) at fixed angles near 90° for a third sample, S3.

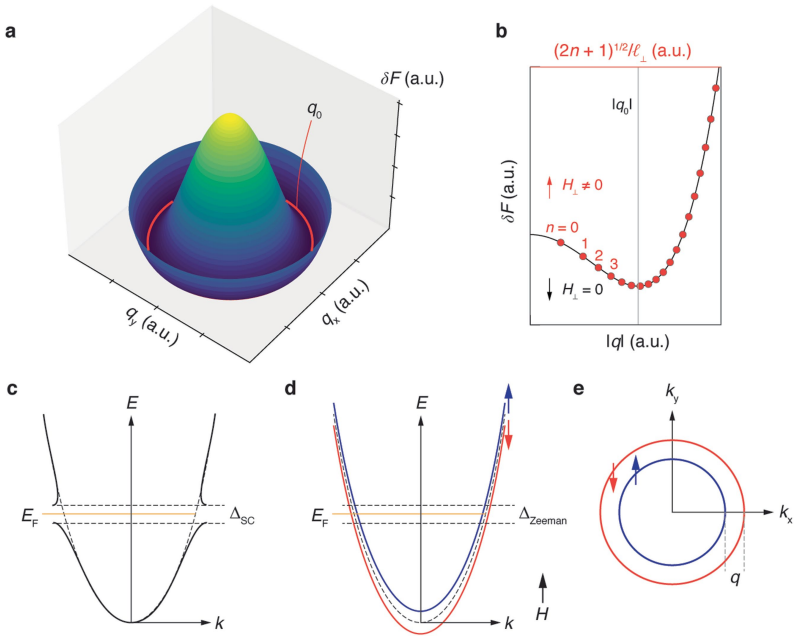

Extended Data Fig. 6 | Ginzburg-Landau modeling. a GL free energy $\delta F(q_x, q_y)$ in the finite-q pairing state of an isotropic superconductor. Finite-q pairing with $|\boldsymbol{q}| = q_0$ minimizes δF (red contour). **b** (black line) Radial cut of $\delta F(q)$ for $H_\perp = 0$. (orange points) For $H_\perp \neq 0$, discrete LLs are formed. The LL with $(2n+1)^{1/2}/\ell_\perp$ closest to q_0 is the optimal solution. **c** Superconductivity opens a gap Δ_{SC} around the Fermi energy E_F (orange). **d** Magnetic field causes Zeeman splitting of a spin-degenerate band (dashed) into spin-up (blue) and spin-down (red) bands. **e** Zeeman split bands create two Fermi surface contours in k-space separated by q.

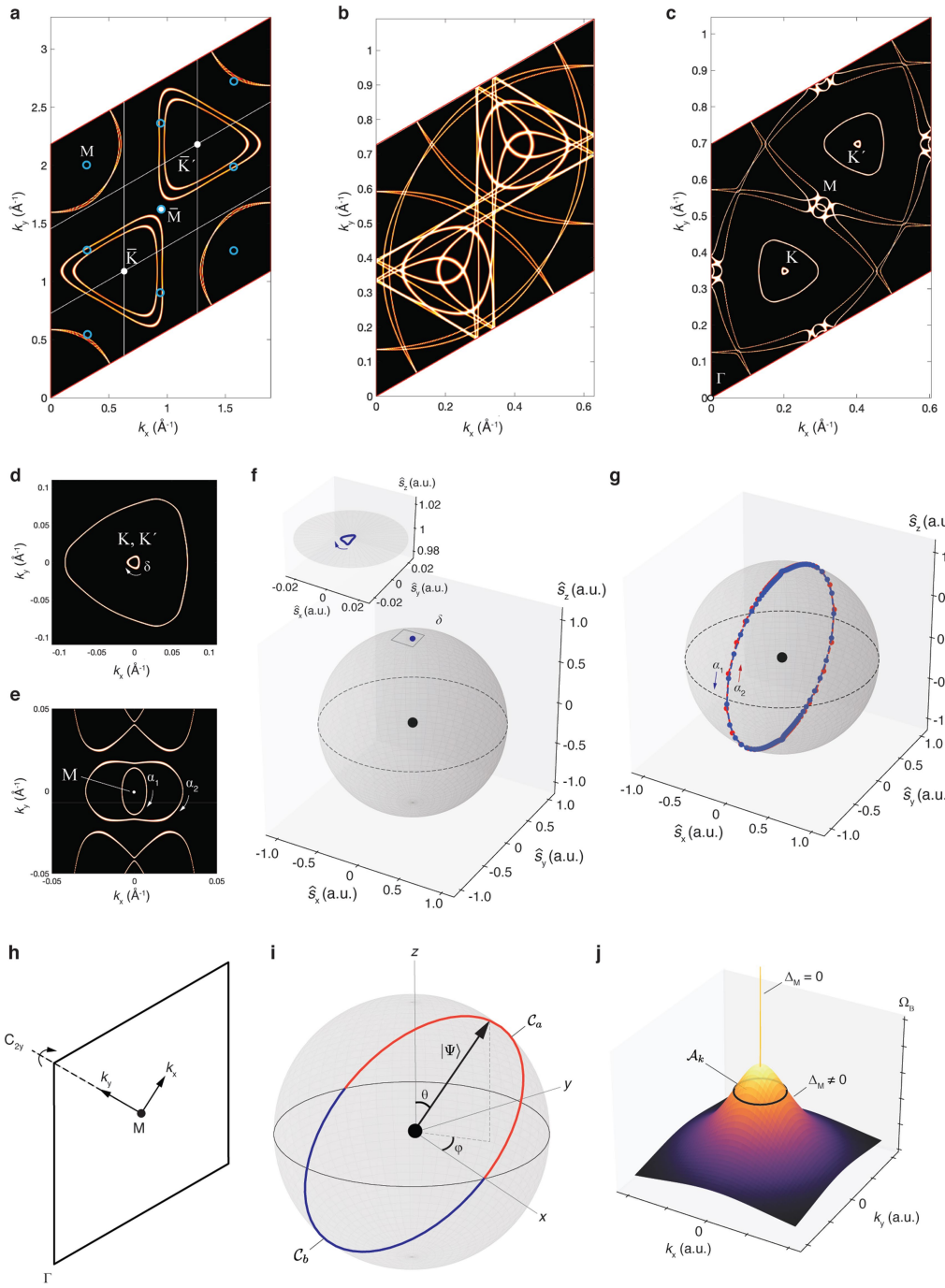

Extended Data Fig. 7 | Electronic structure modeling. a The Fermi surface contours for monolayer *H*-NbS_2. The supercell Brillouin zones and corresponding M points are shown as white lines and open blue circles, respectively. **b** Electronic structure resulting from 3 × 3 zone-folding. This is formed by overlapping the nine cells marked by white lines in (a). **c** Fermi surface contours from first-principles calculations capturing monolayer *H*-NbS_2 and the spacer layer 3 × 3 perturbation. This resembles (b) but with additional band gaps and renormalization due to the spacer layer perturbation. **d** Electronic structure around K, K′ from first-principles with the δ pocket corresponding to f_δ identified. **e** Electronic structure around M from first-principles showing the inner α_1 and outer α_2 pockets. **f** Bloch sphere showing spin-texture along the δ pocket. (inset) Expanded view near the north pole of the Bloch sphere. Blue arrow shows sense of spin evolution for clockwise motion along the δ pocket, see white arrow in (d). **g** Bloch sphere showing spin-texture along the α_1 (blue) and α_2 (red) pockets. Blue (red) arrow shows sense of spin evolution for clockwise motion along the α_1 (α_2) pocket, see white arrows in (e). **h** Coordinate system used for M point **k**·**p** model. **i** Bloch sphere showing the segments $\mathcal{C}_a$ (red) and $\mathcal{C}_b$ (blue) traced by the spin-1/2 eigenvector $|\Psi\rangle$ which together form a closed contour $\mathcal{C}$. **j** Berry curvature $\Omega_B(k_x,k_y)$. For $\Delta_M \neq 0$, Ω_B integrated over the area $\mathcal{A}_k$ defined by the FS contour yields $\varphi_B \neq \pi$.

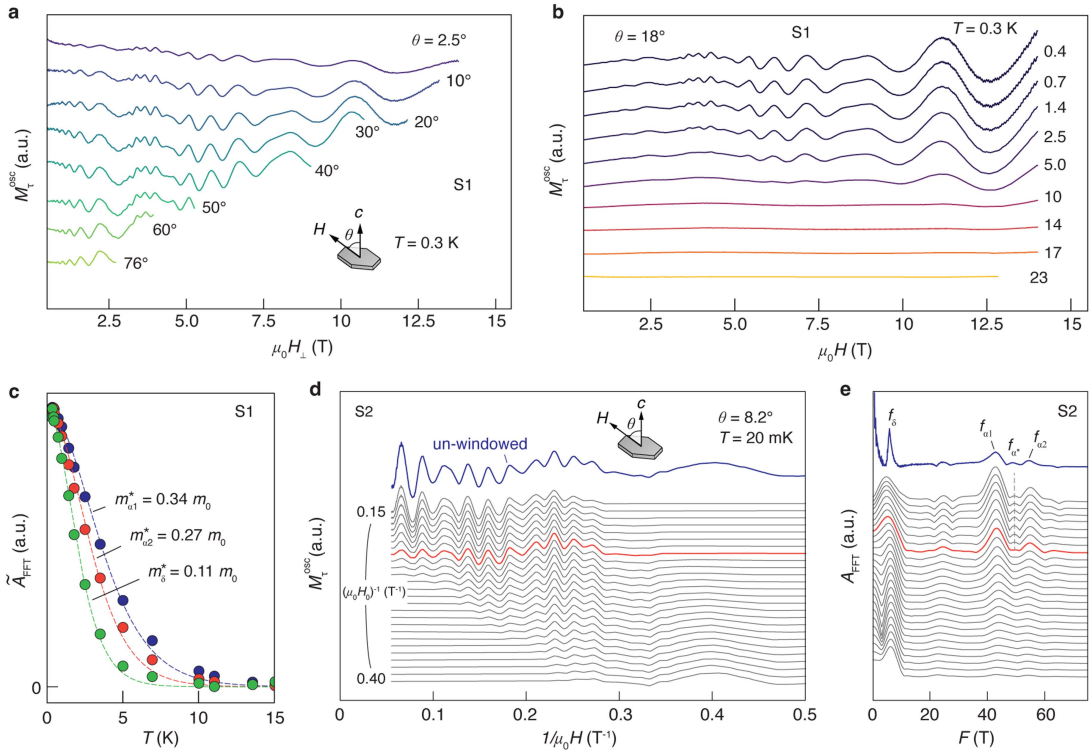

Extended Data Fig. 8 | de Haas-van Alphen oscillations. a $M_\tau^{osc}(H_\perp)$ at $T = 0.3$ K for various angles. The oscillations are aligned across 75° when plotted versus $H_\perp$ indicating the two-dimensionality of the FSs. **b** $M_\tau^{osc}(H)$ at $\theta = 18°$ for various temperatures. **c** $\tilde{A}_{FFT}(T)$ for the α and δ oscillations (points) with fits to R_T^i (Methods) to extract the effective mass. **d** $M_\tau^{osc}(1/H)$ measured at $T = 20$ mK for $\theta = 8.2°$ (blue). The result of applying a sliding window centered at various equally spaced $1/H_0$ are shown as gray and orange traces, vertically offset for clarity. **e** FFT of un-windowed (blue) and windowed (gray) $M_\tau^{osc}(1/H)$ in (d), vertically offset for clarity. The peak at f_{α^*} (grey dashed guide) appears for $1/\mu_0 H_0 < 0.21$ T^{-1}, orange trace in (d) and (e).

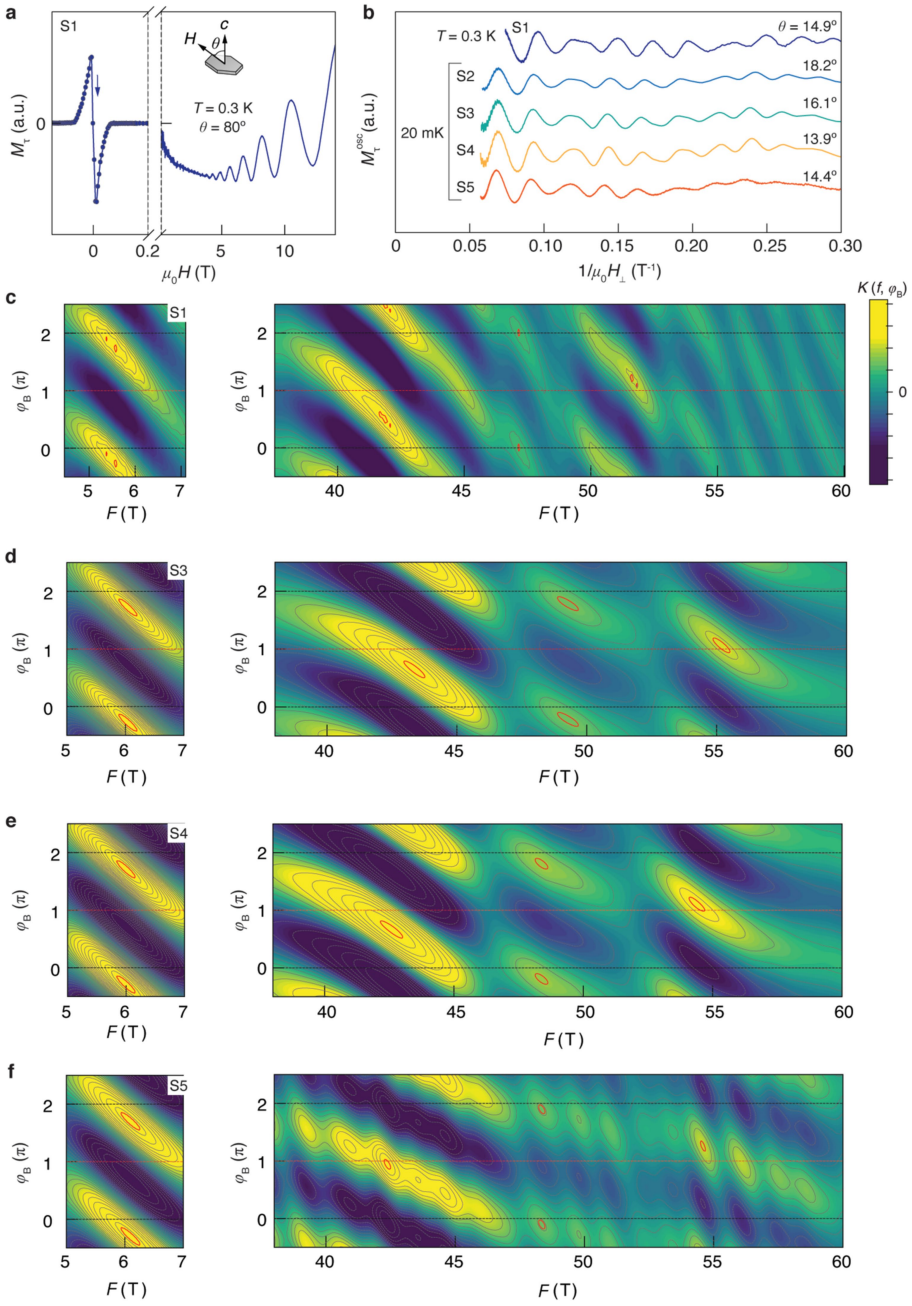

Extended Data Fig. 9 | Phase analysis. a $M_\tau(H)$ measured at $T = 0.3$ K and $\theta = 80°$ showing both the Meissner effect (left) and dHvA quantum oscillation (right). **b** M_τ^{osc} $(1/H_\perp)$ at $T = 0.3$ K ($T = 20$ mK) for sample(s) S1 (S4-S5) at angles near $\theta = 16°$. **c-f** Phase-shift function $K(f, \varphi_B)$ around the δ (left) and α (right) oscillations for samples S1, S3, S4, and S5 using M_τ^{osc} shown in (b). The red contours are drawn at 98% of the local maxima. $K(f, \varphi_B)$ for S2 is shown in Fig. 4b.

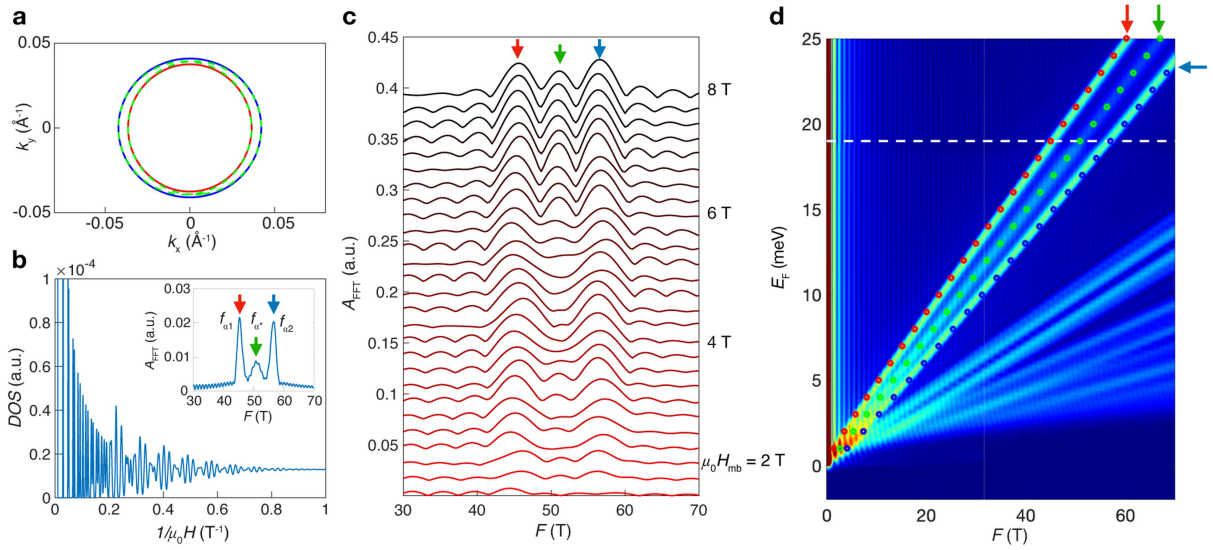

Extended Data Fig. 10 | Calculated Landau level spectrum. a M-point pockets resulting from the **k·p** model with the experimentally determined SOC parameters. The inner (outer) contour in red (blue) corresponds to the measured f_{α_1} (f_{α_2}) frequency. The intersecting dashed green circles are the contours in the presence of mirror symmetry. **b** Calculated density of states in the presence of H showing oscillations due to Landau quantization of the electronic structure in (a). (inset) FFT power spectrum shows three modes corresponding to f_{α_1} (red), f_{α_2} (blue), and the breakdown frequency f_{α^*} (green). **c** The breakdown contribution at f_{α^*} in the FFT power spectrum vanishes at $\mu_0 H_{mb} \approx 6$ T. **d** FFT power spectrum at various values of the chemical potential E_F showing a Landau fan. By comparing with the observed pocket sizes, we can estimate E_F.